eLife

Reviewed Preprint
v1 • September 3, 2026
Not revised

For correspondence:
husem@mskcc.org

* Equal contribution

Competing interests: J.H.Z. is a consultant and/or receives funding from Tanabe Pharma, Hoth Therapeutics, Arcutis Pharma, AmorePacific, and Kiehl's.

Funding: See page 33

Reviewing editor: Rachel Evans, King's College London, United Kingdom

Cutaneous inflammation accelerates the premalignant expansion of melanocytes bearing oncogenic mutations

Diana Tran[1], Anastasiia Vaska[2,*], Tyler El Rayes[2,*], Natalie Lovinger[2], Yassmin A Elbanna[3], Esther Lee[1], Christin E Burd[4], Jonathan H Zippin[5], Morgan Huse[2]

[1]Immunology and Microbial Pathogenesis Program, Weill Cornell Graduate School of Medical Sciences, New York, United States • [2]Immunology Program, Memorial Sloan Kettering Cancer Center, New York, United States • [3]Louis V. Gerstner, Jr., Graduate School of Biomedical Sciences, Memorial Sloan Kettering Cancer Center, New York, United States • [4]Departments of Molecular Genetics, Cancer Biology, and Genetics, The Ohio State University, Columbus, United States • [5]Department of Dermatology, Weill Cornell Medical College, New York, United States

eLife Assessment

This is an **important** work, using preclinical models and reporting that a shared inflammatory and vascular leakage response following Treg depletion, UVB irradiation, and DNFB contact hypersensitivity facilitates outgrowth of premalignant melanocytes. However, some of the work to support the claims is **incomplete**; this pertains particularly to the quantification of melanocyte expansion and sample size inconsistencies. With some additional supporting evidence to strengthen the claims, the study will be of broad interest to cancer biologists and immunologists.

https://doi.org/10.7554/eLife.112061.1.sa3

Abstract

How the cutaneous microenvironment influences early melanomagenesis is poorly understood. Here, we assessed the effects of three immune perturbations on premalignant melanocyte expansion in an autochthonous mouse model of disease. Depletion of regulatory T (T_{reg}) cells markedly accelerated melanoproliferation, an unexpected phenotype that was associated with monocyte and macrophage infiltration, the production of inflammatory and angiogenic factors, and vascular leakage. In line with these observations, single cell transcriptomic analysis of T_{reg} cell deficient skin revealed robust accumulation of monocyte-derived macrophages with tissue remodeling characteristics. Acute UV irradiation and 2,4-dinitrofluorobenzene (DNFB)-induced contact hypersensitivity had analogous effects on both the cellular microenvironment of the skin and the expansion of local premalignant melanocytes. Treatment with the anti-inflammatory agent dexamethasone attenuated DNFB-induced melanocyte expansion and vascular remodeling. Collectively, these results identify a conserved inflammatory axis linked to the early outgrowth of oncogenic melanocytes in the skin.

Introduction

Melanoma is the most lethal form of skin cancer, accounting for approximately 75% of skin cancer–related deaths[1,2]. It develops through the malignant transformation of melanocytes, which proliferate uncontrollably and acquire metastatic potential[3]. Whereas numerous targeted small molecule inhibitors and immune-activating therapeutics are FDA approved to treat metastatic disease, only 50% of patients achieve durable response[4]. Thus, it is critical to better understand the development of melanoma to identify improved methods for diagnosis and treatment. Among

the major drivers of melanomagenesis are activating somatic mutations in *NRAS* and *BRAF*, which are often coupled with loss-of-function mutations in tumor suppressors like *TP53* and *PTEN*[5,6]. However, these same genetic alterations are found in benign melanocytic nevi[7–10], implying that factors other than oncogenic melanocyte mutations are also necessary for malignant progression.

The immune system represents an obvious source for melanocyte-extrinsic determinants of melanoma. Multiple immune cell types, including natural killer cells and $CD8^+$ cytotoxic T lymphocytes, destroy cancer cells directly, and this anti-tumor activity is widely thought to eliminate many nascent tumors before they become clinically detectable[11,12]. Anti-tumor immunity is particularly relevant for melanoma, which can be successfully treated with immune checkpoint blockade (ICB) antibodies that act by derepressing existing clones of tumor-specific T cells[13,14]. Accordingly, the capacity of mutant melanocytes to overcome or evade anti-tumor lymphocytes would presumably be crucial for their outgrowth in the skin.

Regulatory T (T_{reg}) cells, which are defined by expression of the transcription factor Foxp3, function as critical suppressors of lymphocyte activation in both homeostatic and disease contexts[15]. As such, they represent an intriguing candidate immune evasion mechanism for melanoma. Indeed, multiple lines of evidence link T_{reg} cell activity to melanoma outgrowth. Intratumoral T_{reg} cell accumulation has been associated with disease progression in the clinic, and T_{reg} cell depletion inhibits melanoma outgrowth in transplantable models of the disease[16–19]. However, the role of T_{reg} cells during the early, premalignant stage of melanocyte expansion has not been examined.

Beyond anti-tumor immunity, the immune system can also influence tumor progression via tissue inflammation[12,20]. Inflammatory responses are typically triggered by the release of activating cytokines and chemokines in peripheral tissues[21,22]. This drives the recruitment of a variety of innate immune cells from the blood, among them neutrophils and $Ly6C^+$ monocytes, the latter of which rapidly differentiate into inflammatory macrophages. Infiltrating myeloid cells further amplify the inflammatory milieu and release factors that promote tissue remodeling. A key component of this remodeling response is angiogenesis, a process in which initial vascular destabilization is followed by the sprouting of new vessels[23]. Importantly, myeloid-driven inflammation and angiogenesis have both been shown to support tumor progression by providing the space and nutrients necessary for cancer cell growth[20,23].

The link between inflammation and cancer may be particularly relevant to melanoma because ultraviolet (UV) light, the primary environmental driver of this disease, is known to elicit robust cutaneous inflammation and vascular remodeling[24–26]. UV is canonically thought to drive melanomagenesis by generating oncogenic mutations in melanocyte DNA[6,27–30]. While UV-induced mutations clearly contribute to disease progression, emerging evidence indicates that UV may also promote disease via non-mutagenic pathways[31–35]. Mouse models of melanoma have shown that a single dose of UV is sufficient to induce melanomagenesis with no significant increase in oncogenic UV signature mutations[36,37]. Furthermore, acute high doses of UV (e.g., blistering sunburn) are a more significant risk factor for melanoma than chronic UV exposure[31,38–41], despite presumably generating less oncogenic DNA damage. In light of these data, it is tempting to speculate that inflammatory tissue remodeling induced by UV light might create local conditions that are conducive to melanomagenesis. Intriguingly, UV-induced inflammation is also associated with cutaneous T_{reg} cell expansion and the suppression of adaptive immunity in the skin[42–44]. Hence, UV could support melanoma outgrowth by driving both tissue remodeling and immune suppression.

To study the interplay between incipient melanoma and cutaneous inflammation, we subjected an autochthonous murine model of melanoma (*LSL-Braf^{V600E};Pten$^{fl/fl}$;Tyr::CreERT2* mice) to three distinct inflammatory immune perturbations: transient T_{reg} cell depletion, acute UV-B irradiation, and 2,4-dinitrofluorobenzene (DNFB)-induced contact hypersensitivity. Each of these perturbations accelerated premalignant melanocyte outgrowth, which was unexpected given that both T_{reg} cell depletion and DNFB treatment markedly enhanced conventional T (T_{conv}) cell infiltration into the skin. Detailed analysis of each inflammatory response revealed a shared cellular and molecular signature comprising myeloid infiltration, characteristic cytokines and

tissue remodeling factors, and vascular permeability. Importantly, pharmacological suppression of this inflammatory signature mitigated melanocyte expansion, indicating that it plays a central role in early disease progression. These results are consistent with a model in which oncogenic mutation synergizes with tissue destabilization to drive melanomagenesis.

Results

Accumulation of T_{reg} cells in early melanoproliferative lesions

To explore early interactions between oncogene-containing melanocytes and the cutaneous immune system, we employed an established autochthonous model of melanoma: *LSL-Braf^{V600E};Pten$^{fl/fl}$;Tyr::CreERT2* (*BPT*) mice[45]. Topical treatment of these animals with 4-hydroxytamoxifen (4-HT) induces the expression of oncogenic Braf^{V600E} concomitantly with the deletion of the tumor suppressor Pten in melanocytes, which proceed over the ensuing ~8 weeks to form melanoma. We focused on the glabrous skin of the mouse ear because it is conducive to intravital microscopy and because it closely mimics the architecture of human skin.

Our initial studies utilized *BPT* mice bearing an *LSL-TdTomato* allele, which generate TdTomato$^+$ melanocytes after 4-HT treatment. This labelling strategy was selected to facilitate the imaging of melanocytes *in situ* and to enable detection of melanocytic material uptake by immune cells[46]. *BPT;LSL-TdTomato* mice, along with *Tyr::CreER;LSL-TdTomato* controls lacking tumorigenic alleles, were subjected to 4-HT ear painting, and immune cells in the ear skin and the draining lymph nodes (dLN) were analyzed by flow cytometry 35 days later (Fig. 1A, Fig. 1 - supplement 1A-B). At this time point, *BPT* mice exhibited substantial skin darkening due to melanocyte outgrowth, but they had not yet developed obvious tumors (Fig. 1A). Multiple CD45$^+$ immune cell types were enriched in *BPT* ears relative to wild type controls, including T cells (CD3$^+$), monocytes (CD11b$^+$Ly6G$^-$F4/80$^+$MHCII$^-$CCR2$^+$), and macrophages (CD11b$^+$Ly6G$^-$F4/80$^+$) (Fig. 1B). Conventional type I (CD11c$^+$MHCII$^+$F4/80$^-$CD103$^+$CD11b$^-$) and type II (CD11c$^+$MHCII$^+$F4/80$^-$CD103$^-$CD11b$^+$) dendritic cells (cDC1 and cDC2) were also more abundant in BPT skin (Fig. 1C). Infiltrating T cells were predominantly CD4$^+$, with only small numbers of CD8$^+$ T cells detected (Fig. 1B). Notably, approximately one quarter of CD4$^+$ T cells in BPT skin expressed Foxp3, indicative of a substantive T_{reg} cell response (Fig. 1B). Increased T_{conv} and T_{reg} cell numbers were also observed in the *BPT* dLN, but these changes were more modest and fell short of statistical significance (Fig. 1 - supplement 1C-D).

To assess the antigen presentation pathway underlying the enhanced T cell infiltration observed in *BPT* skin, we quantified TdTomato fluorescence in patrolling DC subsets. Little to no TdTomato uptake was observed in control mice, despite the fact that the unmutated melanocytes in these animals were TdTomato$^+$. By contrast, ~50% of cutaneous cDC1s and ~80% of cDC2s in *BPT* ears contained melanocyte material (Fig. 1C). A substantial number of TdTomato$^+$ cDC1s and cDC2s were also observed in the dLNs of 4-HT-treated *BPT* mice (Fig. 1 - supplement 1D), implying that both subsets were potentially capable of presenting mutant melanocyte antigen to naive T cells. To explore a potential basis for melanocyte sampling by DCs, we reconstituted *BPT;LSL-TdTomato* mice with *CD11c-YFP* bone marrow, enabling simultaneous two-photon imaging of YFP$^+$ DCs and TdTomato$^+$ melanocytes in premalignant ears (Fig. 1D). In these experiments, DCs initiated contact with melanocytes within three days of 4-HT treatment, and their interaction frequency trended upward over time as the melanocytes expanded (Fig. 1E). Hence, cutaneous DCs take up material from mutant melanocytes and traffic it to the dLN. Taken together with the increased accumulation of cutaneous T_{conv} cells in premalignant BPT skin, these results suggest that melanocyte specific T_{conv} and T_{reg} cells may be primed in the early stages of mutant melanocyte outgrowth.

T_{reg} cells restrain oncogenic melanocyte outgrowth in the skin

The influx of both T_{conv} and T_{reg} cells into *BPT* skin led us to hypothesize that anti-melanocyte responses mediated by the former might be suppressed by the latter. To test this hypothesis, we prepared *BPT* mice containing the *Foxp3-DTR* allele, which drives diphtheria toxin (DT) receptor

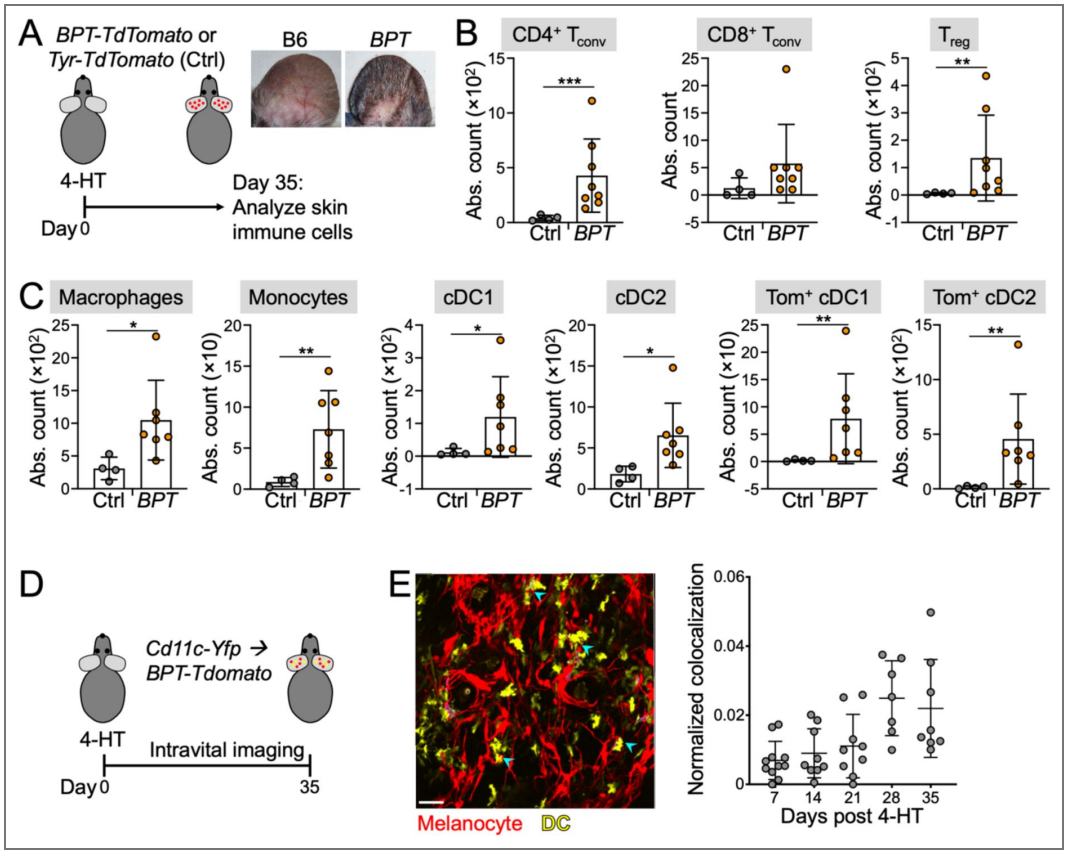

Figure 1. Premalignant melanocyte outgrowth is accompanied by cutaneous immune infiltration.

(A-C) *BPT-TdTomato* and *Tyr-TdTomato* control mice were 4-HT-painted and CD45$^+$ cells in the skin enumerated after 35 days by flow cytometry. (A) Schematic diagram of the experimental approach. Insets show representative melanoproliferation in *BPT* ears 1 month after 4-HT painting. (B) Quantification of the indicated T cell subsets. (C) Quantification of the indicated myeloid cell subsets. Tom$^+$ = TdTomato positive. In B and C, *, **, and *** denote $P \leq 0.05$, $P < 0.01$, and $P < 0.001$, respectively, calculated by lognormal Welch's t-test, except in the case of Tom$^+$ cDC1 and Tom$^+$ cDC2, where Mann-Whitney test was applied. (D-E) *BPT-TdTomato* mice reconstituted with *Cd11c-yfp* bone marrow were 4-HT-painted and subjected to weekly two-photon imaging for 35 days. (D) Schematic diagram of the experimental approach. (E) Representative image of mutant melanocytes (red) and DCs (yellow) in the skin, with DC-melanocyte interactions indicated by cyan arrowheads. Scale bar = 50 μm. (F) Quantification of DC-melanocyte interaction frequency, normalized to the total number of DCs in each image. Error bars denote SD.

expression in T_{reg} cells and thereby sensitizes them to transient depletion by DT[47]. In our experiments, T_{reg} cells were depleted with three injections of DT delivered at 48-hour intervals. This treatment scheme reduced circulating T_{reg} cells to background levels for at least 10 days (Fig. 2 - supplement 1A-B). Cohorts of *BPT;Foxp3-DTR* animals were subjected to three different T_{reg} cell depletion regimens, starting six days before (early), two days after (intermediate), or eight days after (late) 4-HT painting (Fig. 2A). Surprisingly, none of these regimens inhibited 4-HT-induced melanoproliferation. Instead, we found that T_{reg} cell depletion, and in particular early T_{reg} cell depletion, enhanced the outgrowth response, which we visualized photographically and quantified by qRT-PCR of the melanocyte-specific marker *Tyrp1* (Fig. 2B-C). These results indicate that T_{reg} cells constrain premalignant melanocyte expansion during a temporal window closely aligned with the induction of tumorigenic mutations.

In light of these unexpected findings, we re-examined the role of T_{reg} cells in transplantable models of tumor growth. Subcutaneous (s.c.) implantation of syngeneic B16F10 melanoma cells is widely used to study anti-tumor immunity, and it has been applied previously to interrogate the effects of T_{reg} cells on tumor suppression[16,18,19]. To implement early stage T_{reg} cell depletion in the B16F10 system, *Foxp3-DTR* and wild type control mice were treated with the three dose DT regimen described above starting six days before B16F10 implantation (Fig. 2D). Transient T_{reg} cell deficiency significantly inhibited B16F10 tumor growth (Fig. 2E), confirming that T_{reg} cells constrain anti-tumor immunity in this model. In line with this interpretation, flow cytometric analysis of infiltrating immune cells in s.c. B16F10 tumors revealed a robust increase in both $CD8^+$ and $CD4^+$ T_{conv} cells in *Foxp3-DTR* animals (Fig. 2 - supplement 1C-D). Next, we performed an analogous set of experiments in mice receiving intravenous injections of B16F10, which leads to the formation of multifocal "metastatic" tumors in the lungs (Fig. 2F). T_{reg} cell depletion prior to B16F10 injection inhibited cancer outgrowth in this context (Fig. 2G), as well. We conclude that T_{reg} cells can both promote and antagonize incipient tumor formation in the skin, with the autochthonous *BPT* model revealing protective functions during early transformation that are either absent or substantially less important in transplantable B16F10 systems.

T_{reg} cell depletion dramatically alters the cutaneous T cell-DC axis

To investigate how T_{reg} cell depletion promotes mutant melanocyte outgrowth in skin, we subjected *BPT;Foxp3-DTR;LSL-TdTomato* mice and *BPT;LSL-TdTomato* controls to early DT treatment (days -6, -4, and -2) and then assessed leukocyte content in the ear and draining lymph node (dLN) eight days after 4-HT painting (Fig. 3A, Fig. 3 - supplement 1A). T_{reg} cell depletion triggered a dramatic influx of multiple immune cell types into the skin, including T_{conv} cells, neutrophils ($CD11b^+Ly6G^+$), monocytes, macrophages, and DCs ($CD11c^+MHCII^+F4/80^-$) (Fig. 3B-C). Skin T_{conv} cell expansion was apparent in both $CD4^+$ and $CD8^+$ compartments, but was much more obvious among $CD4^+$ T_{conv} cells, which accounted for most of the cutaneous T cells at this time point (Fig. 3B). Among DCs, both cDC1 and cDC2 numbers increased, with cDC2s an order of magnitude more abundant than cDC1s in both T_{reg} cell deficient and T_{reg} cell sufficient skin (Fig. 3C). In the dLN, we observed expansion of all myeloid subsets, with more modest changes in T cell numbers (Fig. 3 - supplement 1B). T cell activation, however, as measured by upregulation of CD44 and downregulation of CD62L, was significantly enhanced in both CD4 and CD8 dLN subsets (Fig. 3 - supplement 1C). Upon restimulation with PMA/ionomycin *in vitro*, almost all dLN $CD44^+$ $CD4^+$ T_{conv} cells expressed IL-4, with little to no expression of IL-17 or IFNγ (Fig. 3 - supplement 1D). This observation is in line with prior work indicating that T_{reg} cells constrain an autoimmune T cell response with T_H2 characteristics in the skin[48].

Next, we measured TdTomato fluorescence in each immune cell type to assess uptake of melanocyte antigen. Tumor sampling of this kind was largely restricted to macrophages, cDC1s, and cDC2s (Fig. 3C, Fig. 3 - supplement 1B). While T_{reg} cell depletion did not boost the fraction of $TdTomato^+$ cells in each subset, their absolute numbers rose markedly due to increases in total macrophages and DCs. Notably, $TdTomato^+$ DCs were observed in the dLN as well as the skin, indicative of successful antigen trafficking (Fig. 3 - supplement 1B). Taken together with the increased accumulation of cutaneous T_{conv} cells described above, these results are consistent with

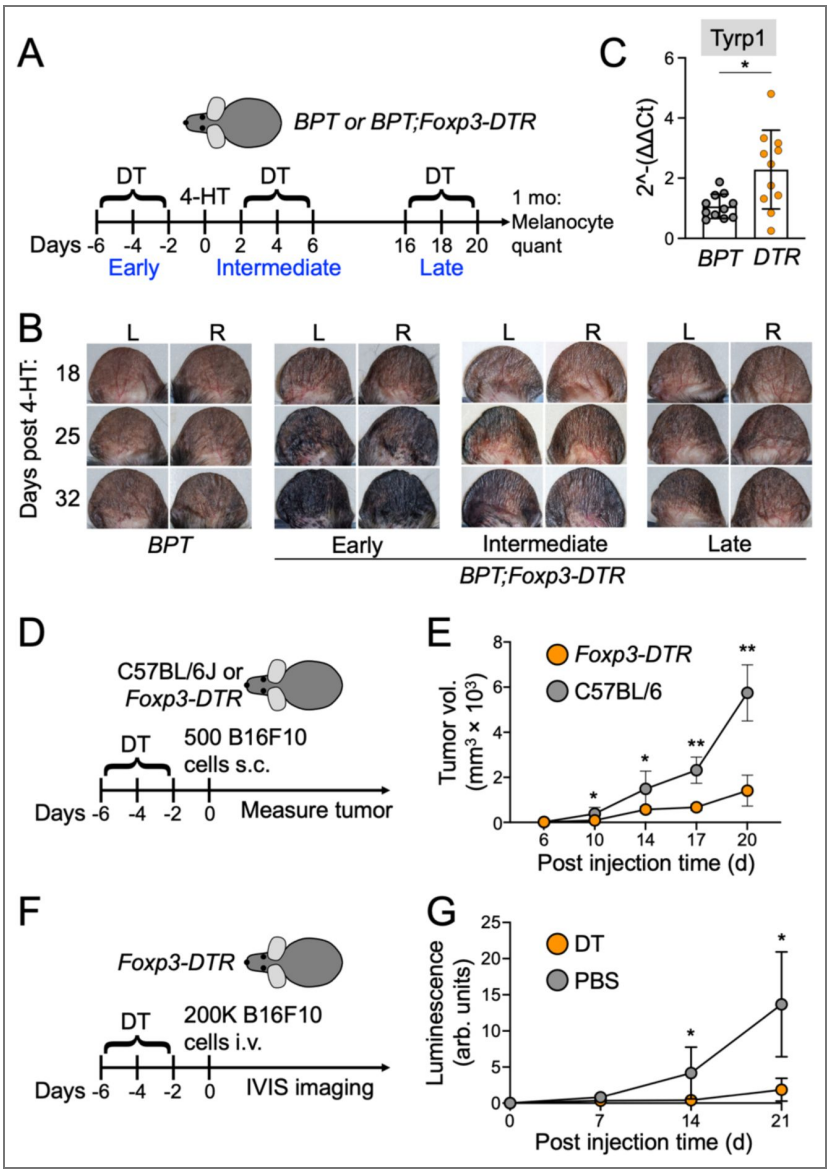

Figure 2. **T_{reg} cell depletion promotes mutant melanocyte outgrowth in the *BPT* model.**

(A-B) *BPT* and *BPT;Foxp3-DTR* mice were subjected to DT treatment either 1 week before (early), just after (intermediate), or 2 weeks after (late) 4-HT painting, and melanocyte outgrowth assessed after 1 month. (A) Schematic of the experimental protocol. (B) Photographs showing representative melanocytic darkening at the indicated timepoints. (C) qRT-PCR quantification of *Tyrp1* expression in ear skin at the experimental endpoint. N = 11 mice per group. Error bars indicate SD. * denotes P ≤ 0.05, calculated by unpaired t-test. (D-E) *Foxp3-DTR* or control (C57BL/6J) mice were treated with DT and then injected s.c. with 500 B16F10 cells. Subsequent tumor growth was measured for three weeks. (D) Schematic diagram of the experimental approach. (E) Quantification of tumor growth, with error bars indicating SD. * and ** denote P ≤ 0.05 and P < 0.01, respectively, calculated by two-way ANOVA. N = 7 mice per group. (F-G) *Foxp3-DTR* mice were treated with DT or vehicle control (PBS), then injected i.v. with 2×10^5 B16F10-Luciferase cells. Subsequent tumor growth was measured for three weeks by IVIS imaging. (F) Schematic diagram of the experimental approach. (G) Quantification of tumor growth, with error bars indicating SD. * denotes P ≤ 0.05, calculated by two-way ANOVA. N = 4 mice per group.

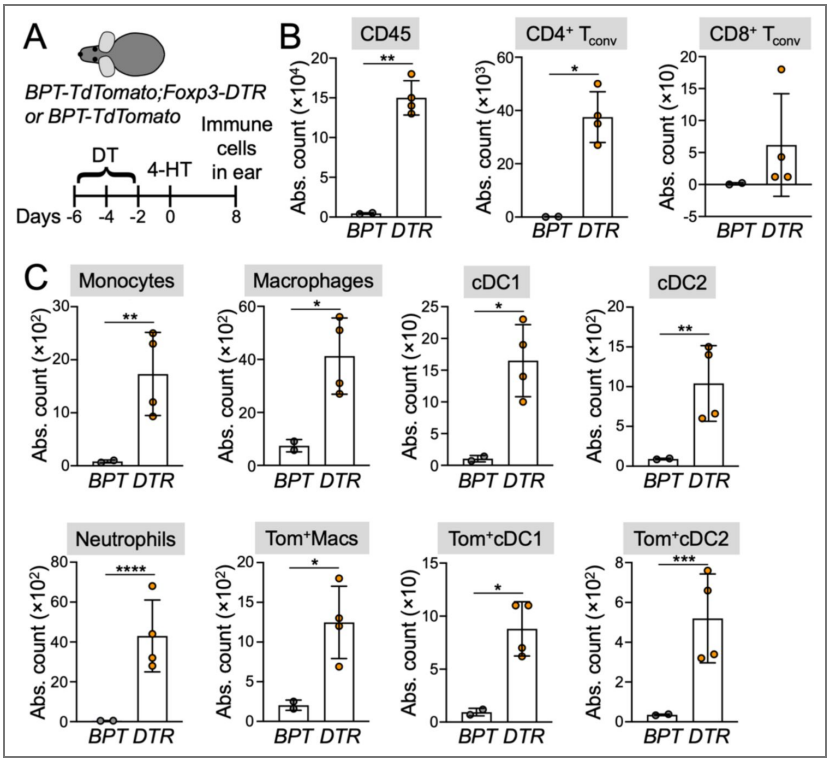

Figure 3. **T_{reg} cell depletion drives multimodal inflammation of the skin.**

BPT-TdTomato;Foxp3-DTR mice and *BPT-TdTomato* controls were treated with DT, followed by 4-HT painting, and immune cells in the ear skin enumerated by flow cytometry after 8 days. (A) Schematic of the experimental protocol. (B) Quantification of the indicated T cell subsets. (C) Quantification of the indicated myeloid cell subsets. Tom^+ = TdTomato positive. In B and C, *, **, ***, and **** denote $P \leq 0.05$, $P < 0.01$, $P < 0.001$, and $P < 0.0001$, respectively, calculated by lognormal Welch's t-test. N = 2 *BPT-TdTomato* mice and 4 *BPT-TdTomato;Foxp3-DTR* mice.

enhanced T_{conv} cell priming and activation in T_{reg} cell deficient skin, which is in line with prior reports[47–49]. What is more surprising is that this immune response failed to antagonize mutant melanocyte outgrowth in the *BPT* model.

T_{reg} cell depletion induces the recruitment of tissue remodeling myeloid cells

To better understand how T_{reg} cells influence the skin microenvironment, we subjected *Foxp3-DTR* mice, along with C57BL/6J controls, to the three dose DT regimen and then profiled $CD45^+$ cells in the ear by scRNA-seq eight days later (Fig. 4A). UMAP analysis of the resulting data revealed drastic differences in immune composition, encompassing both lymphoid and myeloid cells (Fig. 4B). T_{reg} cell depletion dramatically altered the cutaneous T cell compartment, as expected. Whereas control skin was largely devoid of T_{conv} cells, both $CD4^+$ and $CD8^+$ T_{conv} cells were readily apparent in T_{reg} cell-depleted skin (Fig. 4B, Fig. 4 - supplement 1A). *Gzmb* and *Fasl* were robustly expressed among $CD8^+$ T_{conv} cells (Fig. 4 - supplement 1B), indicative of differentiation into armed cytotoxic T cells. $CD4^+$ T_{conv} cells, for their part, exhibited high levels of *Gata3* and *Il4*, but low expression of *Rorc* and *Tbx21*, indicative of a T_H2 response. *Cd69*, *Cd44*, and *Icos* were highly expressed across both subsets, consistent with ongoing T_{conv} cell activation. Collectively, these results suggest that T_{reg} cell depletion unleashes a strong T cell response in the skin, potentially targeting self-antigens or the cutaneous microbiota.

Seurat reclustering of Immgen-defined DCs revealed five clusters of cells whose fractional representations did not change substantially between C57BL/6J and *Foxp3-DTR* mice (Fig. 4 - supplement 1C). Although detailed analysis of individual genes revealed small increases in the expression of activation markers (*CD86* and *CD40*) and class II MHC (*H2-Ab1*) in certain DC clusters (Fig. 4 - supplement 1D), these transcriptional differences were quite modest overall. This was in sharp contrast to the marked increase in total cutaneous DC numbers we observed in T_{reg} cell deficient skin (Fig. 3). Taken together, these results indicate that T_{reg} cell depletion generates predominantly quantitative rather than to qualitative changes in the cutaneous DC compartment.

Conversely, the effects of T_{reg} cell deficiency among monocytes and macrophages were more striking, with several entirely new subsets appearing in the skin at the expense of other populations (Fig. 4C). UMAP replotting of the monocyte/macrophage clusters in the initial all-cell analysis identified two groups of resident cutaneous macrophages in C57BL/6J mice (Fig. 4C, Fig. 4 - supplement 2A). The first (DTR-M-cluster 3) expressed genes characteristic of resident macrophage identity (*Gpr34*, *Ms4a7*, *Pf4*), debris clearance (*Stab1*, *Cd93*), lipid processing (*Apoe*), and tissue maintenance (*Igf1*), implying a role in skin homeostasis. The second subset (DTR-M-cluster 5) exhibited indices of endothelial proximity (*Lyve1*, *Colec12*) and scavenging activity (*Cd209f*, *Cd209g*, *Colec12*), consistent with a resident perivascular macrophage identity.

T_{reg} cell depletion markedly diminished these subsets while inducing the emergence of three additional clusters. The first of these (DTR-M-cluster 4) bore transcriptional signatures characteristic of inflammatory monocytes (*Ly6a*, *Plac8*, *Sell*, *Trem3*, *S100a8*) and interferon signaling (*Ifitm6*, *Vcan*, *Isg15*, *Gbp2*, *Gbp4*). The second cluster (DTR-M-cluster 2) exhibited high levels of transcripts involved in macromolecular processing (*Lgmn*, *Fabp5*) and tissue remodeling (*Mmp14*, *Arg1*). This subset also expressed *Ccl24*, an established chemoattractant for eosinophils, which is consistent with the overall T_H2 character of T_{conv} cells in T_{reg} cell-depleted skin. Importantly, DTR-M-cluster 2 cells also expressed weak but detectable levels of the interferon signaling module seen in DTR-M-cluster 4. Finally, the third cluster (DTR-M-cluster 1) exhibited strong interferon module expression and more modest levels of the inflammatory monocyte and tissue remodeling modules. Taken together, these results were consistent with the ongoing recruitment of inflammatory monocytes (DTR-M-cluster 4) into T_{reg} cell depleted skin and their differentiation into tissue remodeling macrophages (DTR-M-cluster 2) via an inflammatory transitional macrophage subset (DTR-M-cluster 1). Indeed, pseudotime analysis identified a predominant differentiation trajectory starting at DTR-M-cluster 4 and moving sequentially through cluster 1 and then cluster 2 (Fig. 4 - supplement 2B-C). Interestingly, this trajectory then

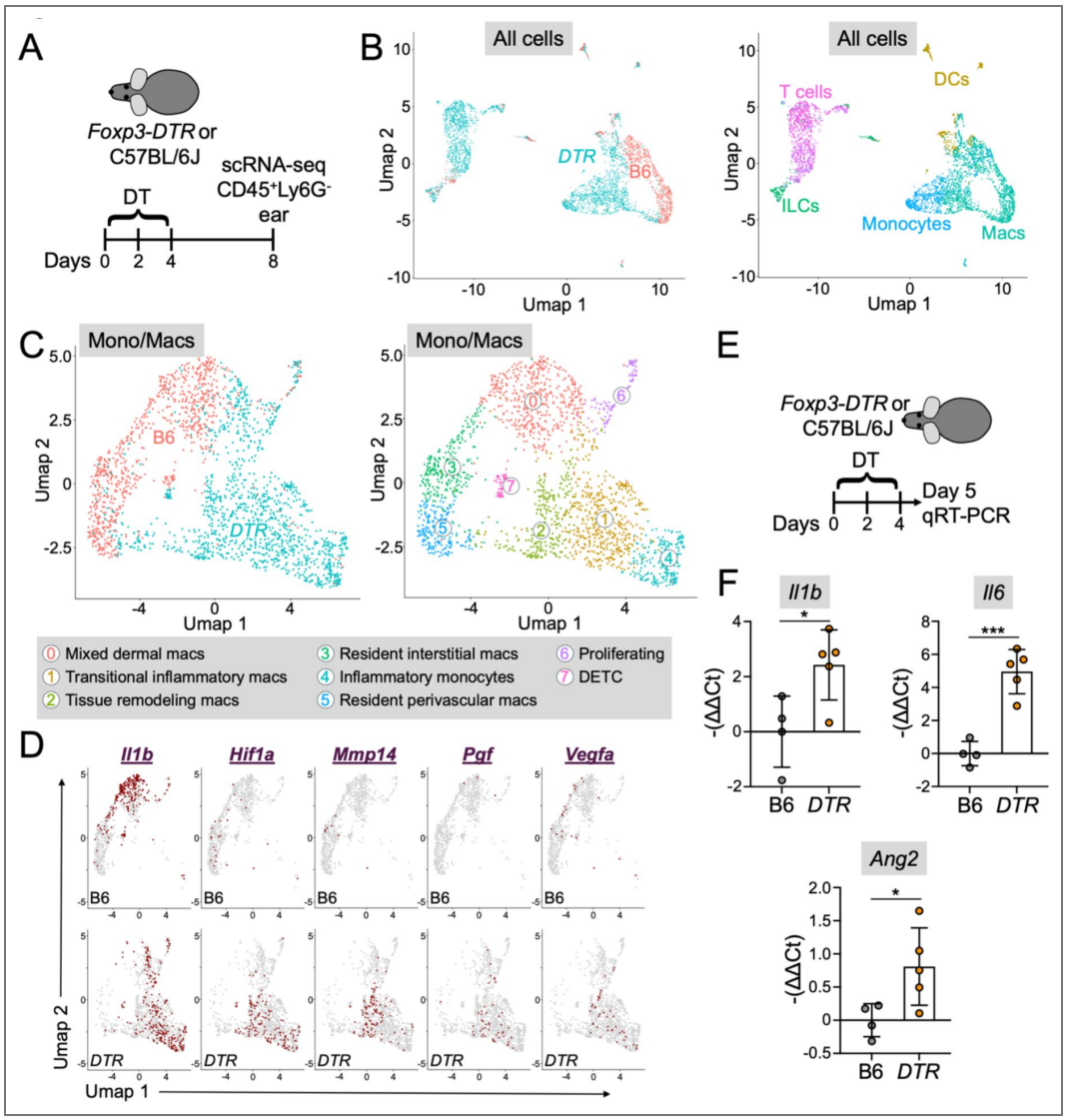

Figure 4. **T_{reg} cell depletion leads to monocyte/macrophage inflammation and tissue remodeling.**

(A-D). $CD45^+$ cells extracted from the ear skin of *Foxp3-DTR* mice or C57BL/6J controls were analyzed by scRNA-seq 8 days after DT treatment. (A) Schematic of the experimental protocol. (B) UMAP showing all sequenced cells from both samples, colored by sample on the left and by cell type on the right. (C) UMAP reclustering of the monocyte and macrophage clusters identified by the UMAP analysis of all cells in B. Cells are colored by sample on the left and by Seurat cluster on the right. The identities of individual Seurat clusters are shown in the legend below. (D) Feature plots of the monocyte/macrophage UMAP showing expression of the indicated inflammatory and tissue remodeling genes in the C57BL/6J (B6) and *Foxp3-DTR* (DTR) samples. (E-F) *Foxp3-DTR* mice and C57BL/6J controls were treated with DT and qRT-PCR performed on skin homogenates 5 days later. (E) Schematic of the experimental protocol. (F) Quantified expression of the indicated genes, with error bars denoting SD. *, **, and *** denote $P \leq 0.05$, $P < 0.01$, and $P < 0.001$, respectively, calculated by unpaired t-test. N = 4 C57BL/6J mice and 5 *Foxp3-DTR* mice.

connected cluster 2 with DTR-M-cluster 0, a macrophage population expressing indices of tissue remodeling (*Mmp12*), lipid metabolism and alternative activation (*Ramp3, Slc27a3*), and immunoregulation (*Cd226, Klrb1b*). Cluster 0 also expressed skin epithelial markers (*Skint3, Hepacam2*), consistent with skin residence or the recent uptake of material from skin resident cells. Notably, cluster 0 was well represented in both *Foxp3-DTR* and C57BL/6J skin, implying that it could be a more long-lived, terminal differentiation state for monocyte-derived macrophages.

Further analysis of the scRNA-seq data revealed elevated expression of stromal remodeling genes, including the hypoxia-induced transcription factor *Hif1a* and the matrix metalloprotease *Mmp14*, by the three monocyte derived subsets (DTR-M-clusters 1, 2, and 4) that emerge in the context of T_{reg} cell deficiency (Fig. 4D). These subsets also displayed increased levels of the angiogenic factors *Vegfa* and *Pgf*, which were only weakly expressed by resident macrophages (DTR-M-clusters 3 and 5). The inflammatory cytokine *Il1b* was robustly expressed by the inflammatory subsets and also by the mixed identity macrophage cluster (DTR-M-cluster 0). This expression pattern would be expected to translate into higher overall *Il1b* production after T_{reg} cell depletion, given the dramatic quantitative increase in cutaneous monocytes and macrophages we observed under these conditions (Fig. 3).

To confirm and extend these results, we subjected *Foxp3-DTR* mice and C57BL/6J controls to the three dose DT regimen and then measured the expression of key inflammatory factors by qRT-PCR five days later (Fig. 4E). T_{reg} cell depletion triggered strong upregulation of both *Il1b* and a second inflammatory cytokine, *Il6* (Fig. 4F). We also documented increased expression of *Ang2*, which encodes a secreted factor that destabilizes the vasculature (Fig. 4F). Taken together with the scRNA-seq data described above, these results document a broad and rapid myeloid inflammatory response in T_{reg} cell deficient skin.

T_{reg} cells maintain vascular homeostasis during premalignant melanomagenesis

The upregulation of angiogenic and blood vessel remodeling factors that we observed in T_{reg} cell deficient skin suggested that these cells might promote vascular stability. To evaluate this hypothesis, we used two photon microscopy to compare cutaneous blood vessel architecture in T_{reg} cell depleted mice with that of healthy controls five days after DT treatment (Fig. 5A). In normal C57BL/6 skin, i.v. injected high molecular weight fluorescent dextran was largely constrained within the vasculature. In *Foxp3-DTR* mice, however, a substantial amount of injected dextran leaked into the surrounding dermal interstitium (Fig. 5B), indicative of vascular permeability. To quantify this vessel destabilization phenotype, we calculated the fraction of dextran-positive area using Z-projection images of the skin. This approach revealed a nearly two-fold increase in the scope of dextran diffusion in T_{reg} cell deficient skin, consistent with a role for these cells in maintaining vascular integrity (Fig. 5C). As an alternative quantification approach, we i.v. injected the mice with the vital dye Evans Blue and then assessed its dissemination into extravascular ear tissue 24 hours later (Fig. 5D). We again found that T_{reg} cell depletion induced a significant, 2-3 fold increase in blood vessel permeability (Fig. 5E).

Next, we examined the interplay between vascular integrity and T_{reg} cells in the context of early tumorigenesis. *BPT;LSL-TdTomato;Foxp3-DTR* mice and *BPT;LSL-TdTomato* controls were subjected to early DT treatment, 4-HT painting, and two-photon imaging with blood vessel tracing performed 30 days after oncogene induction (Figure 5G). $TdTomato^+$ melanocyte expansion was readily apparent in both experimental groups, although more pronounced in *BPT;LSL-TdTomato;Foxp3-DTR* animals, as expected. Importantly, the increased melanocyte load in T_{reg} cell deficient skin was accompanied by severe dextran leakage, which obscured vessel architecture in large regions of tissue (Fig. 5G-H). These results strongly suggest that T_{reg} cells and the inflammatory responses they keep in check control vascular integrity in the premalignant microenvironment.

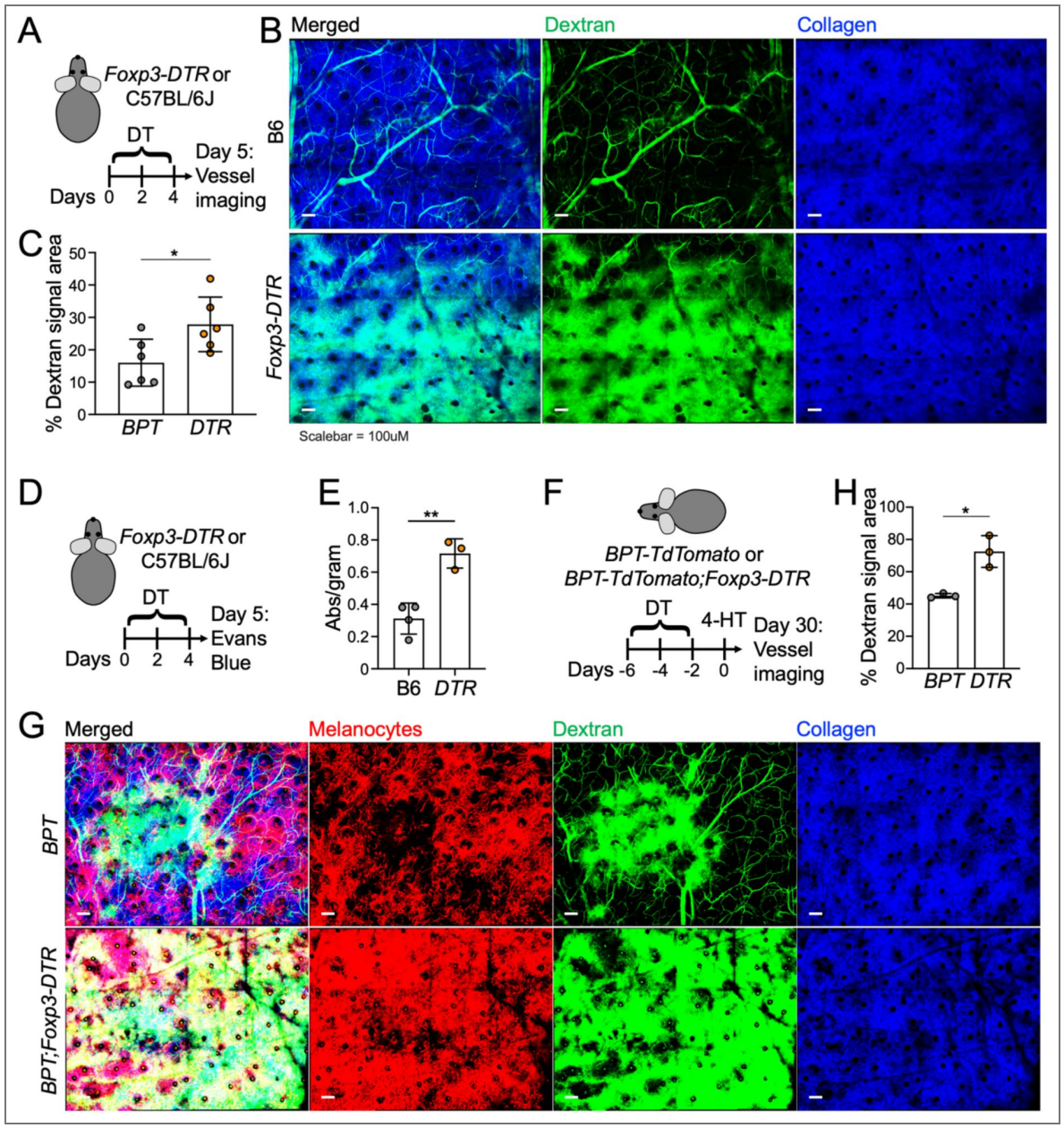

Figure 5. **T_{reg} cell depletion destabilizes vasculature in the skin.**

(A-C) *Foxp3-DTR* mice and C57BL/6J controls were treated with DT and cutaneous vasculature imaged 5 days later by two-photon microscopy after dextran injection. (A) Schematic of the experimental protocol. (B) Representative images of dextran and dermal collagen in C57BL/6J (top) and *Foxp3-DTR* (bottom) skin. Scale bars = 100 μm. (C) Quantification of vascular leakage by fractional area occupied by fluorescent dextran. N = 6 mice per group. (D-E) *Foxp3-DTR* mice and C57BL/6J controls were treated with DT and vasculature leakage in the ears assessed 5 days later by Evans Blue injection. (D) Schematic of the experimental protocol. (E) Quantification of Evans Blue leakage into the skin. N = 4 C57BL/6J (B6) mice and 3 *Foxp3-DTR* mice. (F-H) *BPT-TdTomato* and *BPT-TdTomato;Foxp3-DTR* mice were treated with DT, painted with 4-HT, and then subjected to two-photon imaging after dextran injection 30 days later. (F) Schematic of the experimental protocol. (G) Representative images of dextran, dermal collagen, and TdTomato$^+$ melanocytes in *BPT-TdTomato* (top) and *BPT-TdTomato;Foxp3-DTR* (bottom) skin. Scale bars = 100 μm. (H) Quantification of vascular leakage by fractional area occupied by fluorescent dextran. N = 3 mice per group. All error bars indicate SD. * and ** denote $P \leq 0.05$ and $P < 0.01$, respectively, calculated by unpaired t-test.

UVB radiation drives cutaneous inflammation and premalignant melanocyte expansion

The link between cutaneous inflammation and melanoproliferation that we observed in the context of T_{reg} cell deficiency prompted us to investigate whether other inflammatory stimuli might affect the premalignant microenvironment in similar ways. UV light is the major environmental trigger of human melanoma[38]. Beyond causing DNA damage, UV exposure also induces a potent inflammatory response characterized by macrophage activation, the upregulation of pro-inflammatory mediators, such as IL-1β and TNF [24,50–54], and VEGF production, which contributes to a pro-angiogenic environment[55,56]. Given the similarities between these processes and the effects of T_{reg} cell depletion in the skin, we hypothesized that UV exposure would accelerate tumor progression via analogous mechanisms. To this end, we irradiated the ear skin of *BPT* mice with 2 kJ/m² UVB three days after 4-HT treatment (Fig. 6A). This dose is known to accelerate melanoma progression in autochthonous models, and while it does induce DNA mutations, driver mutations causative for the outgrowth phenotype have not been identified[37]. UVB markedly enhanced the expansion of mutant melanocytes, leading to increased ear darkening and elevated *Tyrp1* expression within a month of oncogene induction (Fig. 6B-C). This outgrowth essentially mirrored the consequences of T_{reg} cell deficiency.

To better understand the microenvironmental effects of UVB in this context, we used qRT-PCR to quantify the expression of inflammatory and angiogenic factors in wild type skin after UV irradiation (Fig. 6D, Fig. 6 - supplement 1A). Within 24 hours of UVB treatment, we observed upregulation of both *Il1b* and *Il6*, along with increased expression of *Vegfa* and *Hif1a* (Fig. 6E). Expression levels of *Il1b* and *Il6* remained high seven days post-UVB (Fig. 6 - supplement 1B). These results indicated that UVB induces a rapid inflammatory and tissue remodeling response in the skin with molecular properties that are similar to the effects of T_{reg} cell depletion. To investigate the cellular basis for this response in more detail, we profiled immune infiltrates in the skin by flow cytometry seven days after UVB treatment (Fig. 6 - supplement 1C). Neutrophil, monocyte, macrophage, and DC levels were all markedly enhanced by UVB (Fig. 6 - supplement 1D). $CD4^+$ T_{conv} cell and T_{reg} cell numbers also increased, which was consistent with prior reports[42,43,57,58], while $CD8^+$ T_{conv} cells remained unchanged (Fig. 6 - supplement 1E). Hence, whereas certain aspects of UVB-induced inflammation mirrored those of T_{reg} cell-depleted skin, other features, most notably the presence of T_{reg} cells themselves, were distinct.

Next, we performed scRNA-seq to profile the diversity of immune cells ($CD45^+$) in the ear skin seven days after 2 kJ/m² UVB irradiation. These cells were predominantly of myeloid lineage, consistent with the flow cytometric results described above (Fig. 6 - supplement 2A-B). The most striking UV-induced changes manifested in the monocyte/macrophage compartment, where two entirely new subsets appeared in irradiated skin (Fig. 6F, Fig. 6 - supplement 2C). These subsets bore a striking resemblance to the monocyte derived populations observed in T_{reg} cell deficient skin (Fig. 4). The first (UV-M-cluster 2) strongly expressed transcripts indicative of inflammatory monocyte identity (*Trem1, Plac8*) and interferon signaling (*Vcan, Ifitm1, Ifitm6*) and more weakly expressed transcripts associated with tissue remodeling (*Spp1, Gpnmb, Mmp14*) and lipid handling (*Fabp5, Apoc2, Hilpda*). This pattern was reversed in the second subset (UV-M-cluster 3), which expressed high levels of the remodeling and lipid handling modules and lower levels of the monocyte and interferon signatures.

Taken together, these results were consistent with UVB-induced recruitment of inflammatory monocytes from the blood, followed by their differentiation into inflammatory, tissue remodeling macrophages. Importantly, *Il1b*, *Mmp14*, *Hif1a*, *Vegfa*, and *Pgf* expression was strong across all UVB-induced subsets (Fig. 6G), suggestive of increased inflammatory and angiogenic activity. To assess this hypothesis directly, we performed intravital blood vessel tracing of ear skin and Evans Blue assays, eight and three days after UVB exposure, respectively (Fig. 6H). These experiments revealed significantly more blood vessel leakage in irradiated ear skin relative to mock-irradiated controls (Fig. 6I-J), consistent with the interpretation that UVB disrupts the cutaneous

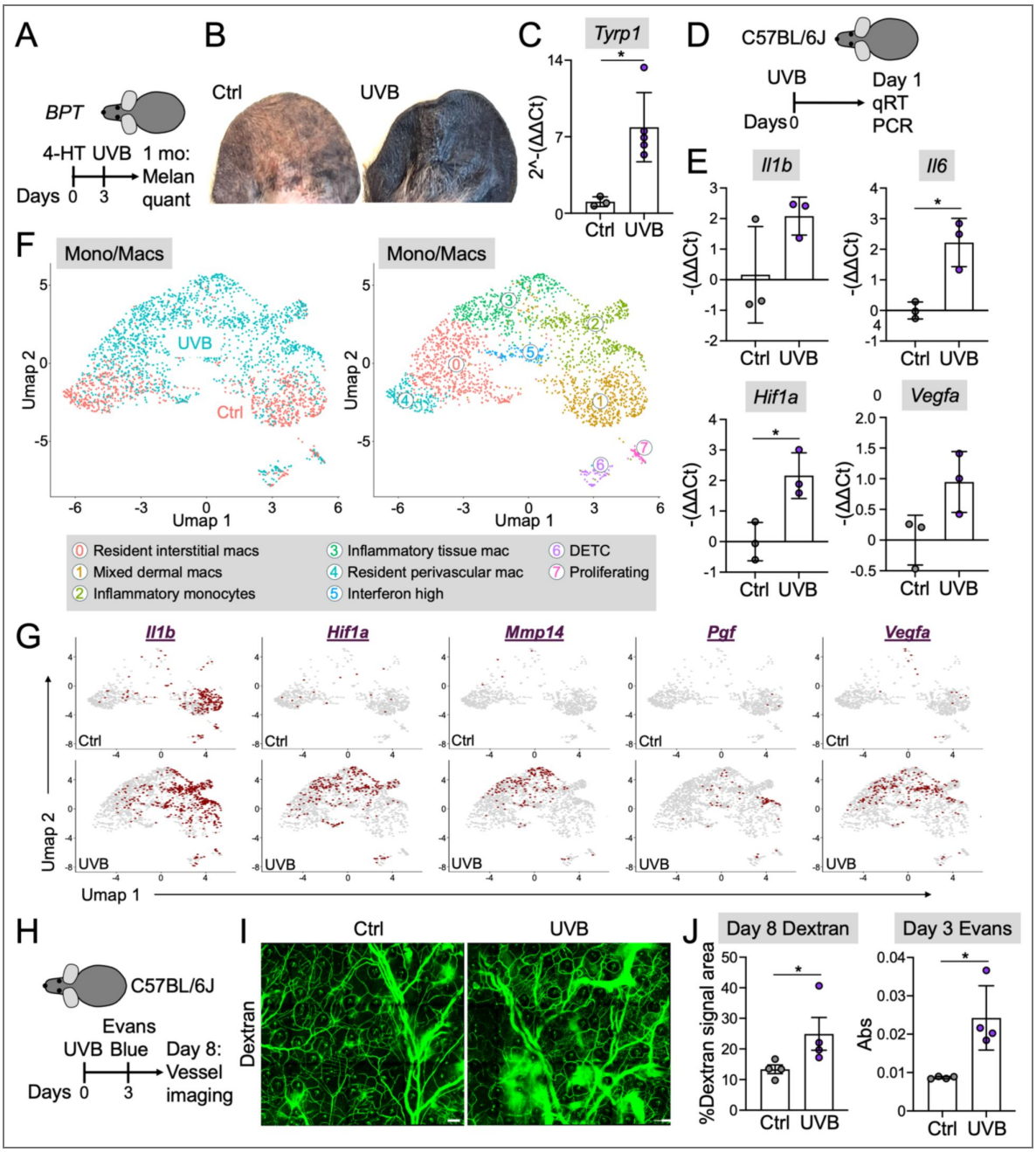

Figure 6. UVB irradiation drives myeloid inflammation and tissue remodeling in the skin.

(A-B) *BPT* mice were UVB irradiated 3 days after 4-HT painting and melanocyte outgrowth assessed at the 30 day timepoint. (A) Schematic of the experimental protocol. (B) Photographs showing representative melanocytic darkening in unirradiated (Ctrl) and UVB-irradiated mice. (C) qRT-PCR quantification of *Tyrp1* expression in ear skin at day 30. N = 3 Ctrl mice and 5 UVB-treated mice. Error bars indicate SD. * denotes P ≤ 0.05, calculated by unpaired t-test. (D-E) C57BL/6J mice were UVB- or mock-irradiated and qRT-PCR performed on skin homogenates one day later. (D) Schematic of the experimental protocol. (E) Quantified expression of the indicated genes. N = 3 mice per group. (F-G) C57BL/6J mice were exposed to UVB or mock irradiation and CD45$^+$ cells from the ear skin analyzed by scRNA-seq 7 days later. (F) UMAP reclustering of the monocyte and macrophage clusters identified by UMAP analysis of all cells (see Fig. 6 - supplement 2). Cells are colored by sample on the left, and by Seurat cluster on the right. The identities of individual Seurat clusters are shown in the legend below. (G) Feature plots of the monocyte/macrophage UMAP showing expression of the indicated inflammatory and tissue remodeling genes in the Ctrl and UVB samples. (H-J) C57BL/6J mice were UVB- or mock-irradiated and cutaneous vasculature integrity assessed 3 days later by Evans Blue injection or 8 days later by two-photon microscopy after dextran injection. (H) Schematic of the experimental protocol. (I) Representative images of dextran in mock- (left) and UVB-irradiated (right) skin. Scale bars = 100 μm. (J) Left, vascular leakage at 8 days post UVB, quantified by fractional area occupied by fluorescent dextran. N = 4 mice per group. Right, quantification of Evans Blue leakage into the skin. N = 4 mice per group. All error bars indicate SD. * denotes P ≤ 0.05, calculated by unpaired t-test.

vasculature. Hence, while UVB-induced skin inflammation differs somewhat from the response to T_{reg} cell depletion, both feature the infiltration of tissue remodeling macrophages and vascular instability.

Contact dermatitis is sufficient to drive dysregulated melanocyte outgrowth

Having demonstrated that an environmental irritant with known immunomodulatory properties (UVB) could induce dysregulated melanocyte outgrowth, we next asked whether a topically applied chemical irritant would have similar effects. 2,4-dinitrofluorobenzene (DNFB) drives potent cutaneous inflammatory responses via covalent modification of skin proteins and other biomolecules, leading to oxidative stress, adaptive immune priming, and type 4 hypersensitivity[59]. We were particularly interested in DNFB because of prior work indicating that it could strongly induce IL-1β and IL-6, a feature we had observed in both UVB-treated and T_{reg} cell deficient skin.

To induce DNFB dependent inflammation, we employed a classical approach in which mice are first sensitized with DNFB on their abdomen and then challenged on one of their ears five days later (Fig. 7A, Fig. 7 - supplement 1A). This protocol induced substantial swelling on the DNFB-treated but not the contralateral, vehicle-treated ear (Fig. 7 - supplement 1B), indicative of strong, DNFB-dependent type 4 hypersensitivity. Using qRT-PCR, we observed dramatic upregulation of *Il1b*, *Il6*, *Hif1a*, and *Ang2* following DNFB elicitation (Fig. 7B). DNFB elicitation also induced marked vascular leakage, as measured by Evans Blue staining (Fig. 7C). Using flow cytometry, we documented a dramatic increase in immune cellularity within two days of DNFB elicitation, encompassing neutrophils, DCs, monocytes, macrophages, and both $CD4^+$ and $CD8^+$ T_{conv} cells (Fig. 7 - supplement 1C-D). Hence, DNFB-induced inflammation recapitulated key characteristics of the immunological responses seen in UVB-treated and T_{reg} cell-depleted skin.

Next, we assessed the capacity of DNFB-induced type 4 inflammation to promote mutant melanocyte outgrowth. BPT mice were sensitized with DNFB, painted with 4-HT on both ears three days later, and then challenged with DNFB on one ear two days after that (Fig. 7D). DNFB-treated ears exhibited substantially more darkening and *Tyrp1* expression than their contralateral counterparts (Fig. 7E), indicative of profoundly dysregulated melanocyte expansion. This DNFB induced effect was similar to but more robust than what we had observed in T_{reg} cell-depleted or UVB-treated mice, prompting us to speculate that it might be capable of promoting melanocyte outgrowth in non-oncogenic conditions. To test this hypothesis, we applied the same experimental protocol to *LSL-Braf^{V600E};Pten$^{fl/+}$;Tyr::CreERT2* (*BT-Het)* mice, which retain one copy of *Pten* (Fig. 7F). *BT-Het* mice fail to develop melanoma after 4-HT treatment, with melanocyte expansion arresting at the nevus stage[45]. DNFB elicitation dramatically accelerated melanocyte outgrowth in these animals (Fig. 7G), suggesting that cutaneous inflammation can drive melanoproliferation even in the absence of tumorigenesis.

Finally, to determine whether cutaneous inflammation was the actual cause of DNFB elicitation-induced melanoproliferation, we treated 4-HT- and DNFB-painted *BPT* mice with dexamethasone (Dex), a powerful immunosuppressive anti-inflammatory drug. Dex was administered both by i.p. injection one hour before DNFB elicitation and in a topical manner concomitantly with DNFB (Fig. 7A, 7D, S7A). In the context of Dex treatment, we observed marked reductions in *Il1b*, *Hif1a*, and *Ang2* expression in DNFB-painted ears (Fig. 7B), which were also less swollen than the corresponding ears on mice receiving no Dex (Fig. 7 - supplement 1B). Interestingly, *Il6* levels were only modestly inhibited by Dex (Fig. 7B). Notwithstanding this mixed effect on inflammatory indices, we observed a substantial reduction in DNFB elicitation-induced melanocyte outgrowth in Dex-treated mice (Fig. 7E), which was accompanied by marked attenuation of the vascular leakage phenotype (Fig. 7C). Taken together, these data demonstrate that type 4 inflammation can drive robust outgrowth of melanocytes, and they also suggest that blood vessel remodeling plays a particularly important role in this process.

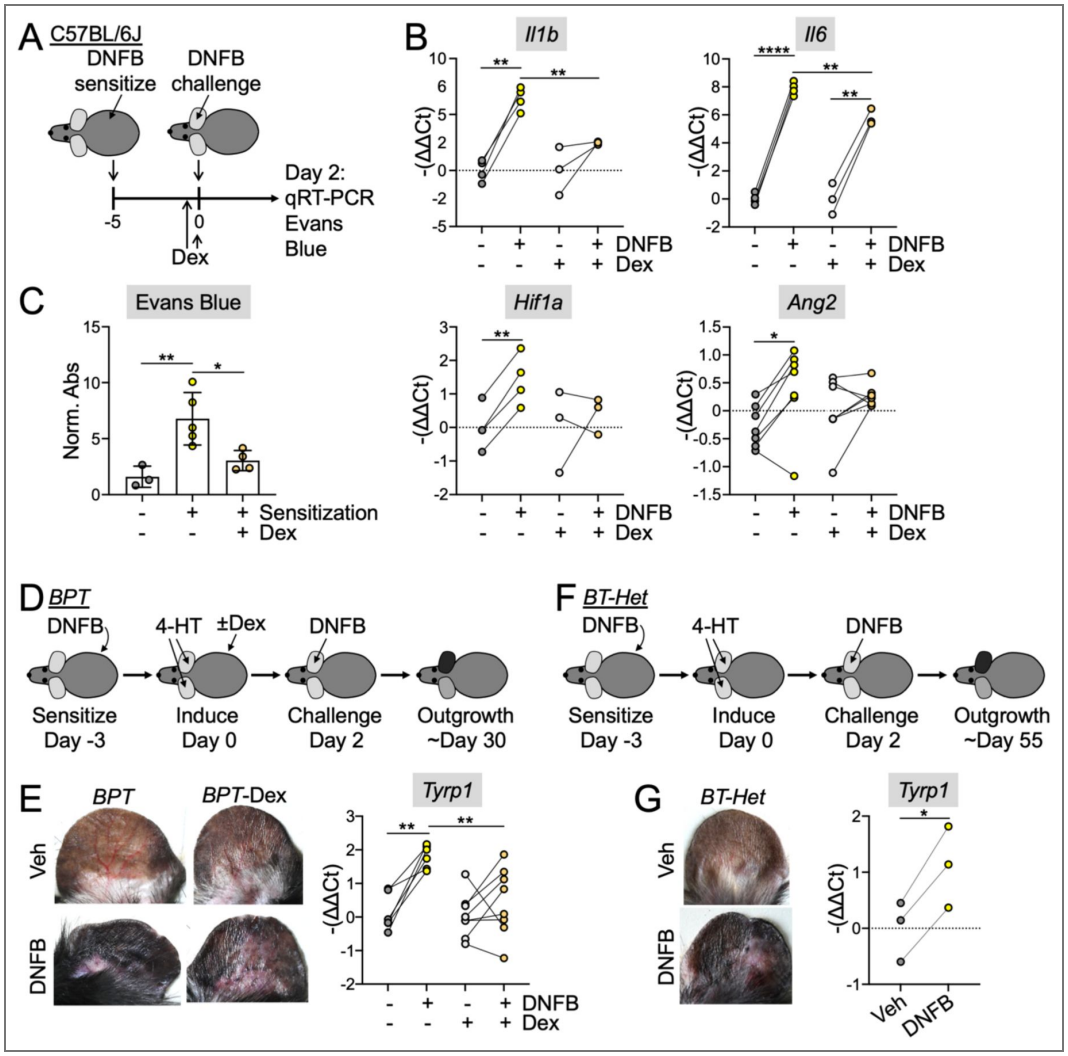

Figure 7. Contact hypersensitivity drives inflammation dependent melanocyte expansion.

(A-C) C57BL/6J mice were sensitized with DNFB and then rechallenged on one ear in the presence or absence of Dex therapy. qRT-PCR analysis of inflammatory genes and Evans Blue analysis of vascular leakage was performed 2 days after elicitation. (A) Schematic of the experimental protocol. (B) Expression of the indicated inflammatory genes was quantified for the indicated DNFB and Dex treatment conditions. N ≥ 3 mice per group. ** and **** denote P < 0.01 and P < 0.0001, respectively, calculated by paired t-test for +/- DNFB comparisons and unpaired t-test for +/- Dex comparisons. (C) Quantification of Evans Blue leakage into the skin. N ≥ 3 mice per group. * and ** denote P ≤ 0.05 and P < 0.01, respectively, calculated by one-way ANOVA. Error bars indicate SD. (D-E) *BPT* mice were sensitized to DNFB, 4-HT-painted on both ears, and then rechallenged with DNFB on one ear in the presence or absence of Dex therapy. Melanocyte outgrowth was quantified photographically and by qRT-PCR 30 days later. (D) Schematic of the experimental protocol. (E) Left, photographs showing representative melanocytic darkening in DNFB- and vehicle-treated ears, with elicitation performed in the presence or absence of Dex. Right, qRT-PCR quantification of *Tyrp1* expression in ear skin at the experimental endpoint. N ≥ 6 mice per group. ** denotes P < 0.01, calculated by paired t-test for +/- DNFB comparisons and unpaired t-test for +/- Dex comparisons. (F-G) *BPT-Het* mice were sensitized to DNFB, 4-HT-painted on both ears, and then rechallenged with DNFB on one ear. Melanocyte outgrowth was quantified photographically and by qRT-PCR 55 days later. (F) Schematic of the experimental protocol. (G) Left, photographs showing representative melanocytic darkening in DNFB- and vehicle-treated ears. Right, qRT-PCR quantification of *Tyrp1* expression in ear skin at the experimental endpoint. N = 3 mice per group. * denotes P ≤ 0.05, calculated by paired t-test.

Discussion

The effects of acute inflammation on the premalignant phase of cancer progression are poorly understood, due in no small part to difficulties in studying early disease using standard transplantable tumor models. To address this issue, we combined the autochthonous *BPT* model with three inflammatory triggers: T_{reg} cell depletion, UVB irradiation, and type 4 hypersensitivity. Strikingly, all three perturbations markedly enhanced the outgrowth of mutant melanocytes, despite the fact that they are known to elicit cutaneous inflammation in mechanistically distinct ways. T_{reg} cell depletion drives systemic T_{conv} cell activation, leading to extensive infiltration of $CD8^+$ T_{conv} cells, $CD4^+$ T_H2 effector cells, and inflammatory myeloid cells into the skin[47,48,60]. DNFB-induced hypersensitivity also drives T_{conv} cell and myeloid inflammation, but the response is more T_H1-skewed and constrained to the skin itself[61]. In contrast, UVB promotes robust cutaneous recruitment of myeloid cells along with $CD4^+$ T_{conv} and T_{reg} cells, but not $CD8^+$ T_{conv} cells[24,25,42,44]. Although the distinct features of these three responses were readily apparent in our experiments, certain critical attributes were shared, including the robust accumulation of inflammatory monocytes and macrophages, increased expression of *Il1b* and *Il6*, and the destabilization of cutaneous vasculature, accompanied by the upregulation of tissue remodeling and angiogenesis programs. *Hif1a*, *Vegfa*, and *Ang2* likely function together within this axis to drive vascular remodeling, promoting vessel destabilization, angiogenesis, and increased permeability. Importantly, reversal of inflammatory tissue remodeling with Dex inhibited DNFB-induced outgrowth of mutant melanocytes. Vascular destabilization and angiogenesis are thought to promote the progression of small tumors into more aggressive and metastatic states[62]. Our results indicate that this “angiogenic switch” may be initiated and/or activated at a much earlier, premalignant stage.

T_{reg} cells are widely thought to facilitate tumor growth by restraining T_{conv} cell responses against tumor-specific antigens[63]. Our findings challenge this view by showing that T_{reg} cell depletion can enhance the outgrowth of mutant melanocytes during the early, premalignant phase of disease progression. This unexpected phenotype is likely caused by dysregulated T_{conv} cell responses against non-melanocytic self-antigens and/or cutaneous microbiota, leading to tissue damage, inflammatory myeloid infiltration, and the tissue remodeling response described above. Additional studies will be required to establish the precise chain of causation. At this stage, however, it seems fair to conclude that T_{reg} cells can exert both pro- and anti-tumorigenic effects on melanoma, depending on the stage of disease progression and on specific microenvironmental features that emerge through the course of tumor growth. In light of our findings, immunotherapeutic efforts centered on the modulation of T_{reg} cell activity should be evaluated with this more holistic conception of T_{reg} cell function in mind.

The inhibition of melanocyte outgrowth by T_{reg} cells in the *BPT* model is particularly striking given prior results from other labs (and our own data) showing that T_{reg} cells play a protumorigenic role in transplantable models of disease[16–19]. Although transplantable systems are easier to implement and quantify, the injection of a bolus of cultured cancer cells, often with additional components like matrigel, disrupts the tissue interactions and stromal-immune crosstalk that define the microenvironment of nascent tumors. The capacity of autochthonous models to recapitulate these microenvironmental features is therefore critical for accurately representing the early, premalignant stage of disease.

It is becoming increasingly clear that UV light can promote melanocyte proliferation and melanoma independently of its capacity to induce oncogenic mutations. We and others have shown that a single dose of UVB is sufficient to promote melanomagenesis and that timing (UVB delivered immediately before or during the formation of driver oncogenes but not after) is critical for generating melanomagenic effects[31,37,39–41]. Taken together, these findings suggest that UV enhances melanoma outgrowth in part by altering the local tumor microenvironment. Our present results lend further support to this idea by closely tying UVB-induced melanocyte expansion to an inflammatory immune response in the skin, which is consistent with prior work showing that acute UVB irradiation promotes the expansion of both oncogenically mutated and

unmutated melanocytes in an inflammation dependent manner[64–66]. Interestingly, two of these studies directly implicated inflammatory macrophages in the melanocyte proliferation response[65,66]. Identifying the UVB-elicited factors underlying myeloid recruitment and also the molecular pathways by which these cells activate melanocytes could reveal new translational avenues for mitigating the oncogenic effects of UV. Notably, UVB-induced inflammation also leads to local T_{reg} cell expansion in the skin, which could facilitate premalignant outgrowth by restraining melanocyte-reactive T_{conv} cell activity. Although the relative importance of myeloid cells *vis-a-vis* T_{reg} cells in this context remains to be determined, our observations that T_{reg} cell depletion and DNFB-induced hypersensitivity both enhance early melanocyte expansion while simultaneously promoting T_{conv} cell activation and infiltration implies a more critical role for myeloid cells in this context.

Regular aspirin use has been associated with reduced melanoma incidence in postmenopausal women[67], implying that anti-inflammatory drugs could potentially be used as a chemoprevention strategy for this disease. While clinical findings like this must be interpreted cautiously, they are consistent with the causal role for inflammatory signaling in early melanomagenesis that our results support. That Dex suppresses DNFB-induced melanocyte outgrowth in our model provides a direct experimental correlate and motivates more targeted investigation of specific anti-inflammatory mediators as potential preventive agents in individuals with elevated melanoma risk.

Our findings that contact hypersensitivity can promote the expansion of non-malignant *BT-Het* melanocytes have interesting implications for benign hyperpigmentation conditions, such as post-inflammatory hyperpigmentation, Riehl's melanosis, and melasma[68–74]. These disorders can lead to significant psychosocial stress, and billions of dollars are spent annually on treatments to reduce excess pigmentation. Post-inflammatory hyperpigmentation and Riehl's melanosis usually occur following T_{conv} cell dependent inflammatory conditions such as atopic dermatitis or allergic contact dermatitis, whereas melasma is associated with exuberant mast cell and T_H2 inflammation. In each case, the condition is defined by increased proliferation of melanocytes leading to increased epidermal pigmentation. In light of our results, it is tempting to speculate that a better understanding of *BT-Het* melanocyte outgrowth in the context of cutaneous inflammation could inform the treatment of both disorders.

While chronic inflammation is an established hallmark of cancer, acute inflammation is often presented as a critical component of anti-tumor immunity. Our results indicate that the cancer cell extrinsic consequences of acute inflammation can have the opposite effect by laying a stromal foundation for premalignant expansion. Whether pro- or anti-tumoral effects predominate in a given situation will likely depend on contextual features such as the structure of the tissue in question, the size and stage of the tumor, and the tone of local immune cells. Identifying these inflammatory determinants could facilitate improved cancer prevention and immunotherapy.

Methods

Mice

The animal protocols used in this study were approved by the Institutional Animal Care and Use Committee of Memorial Sloan Kettering Cancer Center. Unless specified, experimental mice were 8-10 weeks old. All comparative analyses were performed on age- and sex-matched cohorts, which were either male or female. *Foxp3-DTR* mice were kindly provided by A. Y. Rudensky. *BPT* (B6.Cg-Tg(Tyr-cre/ERT2)13Bos;Braf-tm1Mmcm;Pten-tm1Hwu/BosJ), C57BL/6J, *Cd11c-yfp* (B6.Cg-Tg(Itgax-Venus)1Mnz/J), and *LSL-TdTomato* (B6.Cg-Gt(ROSA)26Sor-tm9(CAG-tdTomato)Hze/J) mice were purchased from the Jackson Laboratory. All reported strains and combinations thereof were bred and maintained at Memorial Sloan-Kettering Cancer Center (MSKCC).

T_{reg} Cell Depletion

To achieve sustained T_{reg} cell depletion, a total of three intraperitoneal (i.p.) DT (25 mg/kg) injections were administered to *Foxp3-DTR* mice at 48-hour intervals. T_{reg} cell clearance was verified by flow cytometric quantification of $Foxp3^+$ T cells in the blood.

UVB irradiation

Mice were anesthetized with isoflurane and laid prone on a warming blanket. They were then irradiated with UVB using a Daavlin hand-held broad band (280-320nm filter with sharp cutoff) lamp (5.2 mW/s). The lamp was metered before each irradiation to ensure consistency and distance from mice was maintained at 0 cm. Mock irradiation was conducted using a standard incandescent desk lamp which was confirmed to not emit UVB.

Subcutaneous B16F10 Implantation

500 B16F10 cells were resuspended in RPMI and mixed in a 3:1 ratio with growth factor–reduced matrigel. The sample was then subcutaneously (s.c.) injected in the flank of recipient mice. Subsequent primary tumor outgrowth was monitored by measuring tumor length (L) and width (W). Volume was then calculated as $\pi LW2/6$.

Cell Implantation for Metastasis

200,000 of luciferase expressing B16F10 cells were injected intravenously (i.v., tail vein) into recipient mice. Tumor growth was monitored weekly thereafter by bioluminescent (IVIS) imaging.

Prior to imaging, mice were anesthetized with isoflurane and their thoracoabdominal fur shaved using an electric clipper. D-luciferin (150 mg/kg) was injected retro-orbitally into each mouse, and bioluminescence recorded using an IVIS Spectrum Xenogen instrument (Caliper Life Sciences) equipped with Living Image Software v.2.50. A head-to-tail-base ROI (region of interest) of uniform size was applied to all subjects to measure the total flux (photons/second) of metastatic cancer cells.

4-HT Application

Mice were placed under isoflurane anesthesia, and 32 µg of 4-Hydroxytamoxifen (Sigma, H6278) in DMSO was delivered via micropipette to each ear. Isoflurane was maintained for 15-20 minutes to ensure unhindered absorption of the drug.

DNFB Sensitization and Elicitation

Mice were placed under isoflurane anesthesia, and 25 µL of 0.5% DNFB (1-fluoro-2,4-dinitrobenzene) in 1:4 olive oil:acetone was applied via micropipette to the shaved abdomen. The treated area was allowed to dry for 4 minutes. Hindleg nails were clipped to prevent subsequent scratching of the sensitized site (abdomen). 5 days later, elicitation was performed by applying 10 µL of 0.5% DNFB (1-fluoro-2,4-dinitrobenzene) in 1:4 olive oil:acetone to the right ear and the vehicle mixture to the left ear of each mouse, under isoflurane anesthesia. The treated areas were allowed to dry for 4 minutes before the mice were revived. Hindleg nails were clipped to prevent subsequent scratching of the elicited site (ear).

Dex Treatment of DNFB-Elicited Mice

One hour prior to elicitation, mice were administered Dex by i.p. injection (2.8 mg/kg, with 3:7 PEG400:PBS as vehicle). 0.45% Dex was also combined with the 0.5% DNFB solution (1:4 olive oil:acetone) applied topically to induce elicitation. Control mice received i.p. injection of the vehicle alone and were treated topically with 0.5% DNFB solution in 1:4 olive oil:acetone.

Evans Blue Assay

Isoflurane anesthetized mice were i.v. injected (retro-orbital) with 100 µL of 1% Evans Blue dye in PBS, filtered through 0.45 µm strainer. The mice were euthanized 1.5 hours later, at which point their ears were harvested and placed into 1 mL of formamide for 2 days at 56 °C. Evans Blue levels were then quantified as the difference between absorbance at 620 nm and 720 nm.

Ear Thickness Measurements

Two days post challenge, DNFB-elicited mice were anaesthetized with isoflurane, and their ear thickness was measured using the Dial Thickness Gauge (Mitutoyo, Manufacturer Part Number: 7300A).

Chemical Depilation

Ear skin was depilated 10-14 days prior to the initiation of any experimental protocol. Mice were first anesthetized with isoflurane. Mouse ears were coated with a thin layer of Nair^{TM} and rinsed with PBS following a 4-minute incubation. Ear skin was then dried using a kimwipe. Hind leg nails were clipped to prevent subsequent scratching of the chemically depilated site.

Whole tissue RNA isolation and Quantitative RT-PCR

Ears were harvested from euthanized mice and mechanically homogenized in TRIzol using razor blades, followed by bead lysis. RNA was isolated from the TRIzol mixture in accordance with the TRIzol Reagent User guide (Doc. Part No.15596026.PPS, Pub. No.MAN0001271). The resulting RNA was then purified using the Zymo Research RNA Clean & Concentrator kit per the manufacturer's instructions. RNA purity and concentration were determined using a NanoDrop spectrophotometer. cDNA was synthesized from total RNA and then used as a template for qRT-PCR using the LunaScript® Universal One Step Kit on a StepOnePlus device (Applied Biosystems). mRNA expression levels were normalized to *Gapdh* expression and relative gene expression between samples was calculated using the -ΔΔCt method. Primer sequences are listed in Table 1.

Macroscopic Photography

A NikonZ6 camera fitted with Nikon 1.5 mm macro lens was used to capture all macroscopic images of mouse ears. Photographs were processed using Adobe Lightroom Classic (v14.1.1) and Microsoft PowerPoint. All compared images received identical processing.

Generation of bone marrow (BM) chimeras

BPT;LSL-TdTomato mice were lethally irradiated (900 cGy) using a cesium source and reconstituted with 4×10^6 bone marrow cells derived from *Cd11c-yfp* donor mice. Reconstitution of the hematopoietic compartment was monitored in the blood starting 6 weeks after reconstitution.

Intravital Imaging of Murine Ears

For intravital imaging studies, mice were anaesthetized and maintained on 1.5% isoflurane in 100% oxygen for up to 2 hours. Each mouse was restrained on a stage warmer at 37°C (BioTherm Micro S37; Biogenics) and the ear was mounted onto a custom-made stage for imaging[75]. Two-photon microscopy was performed on an Olympus FVMPE- RS system equipped with a 25× 1.05 NA water immersion objective and a tunable InSight laser. Images were acquired with Fluoview software (FVS31). For experiments using *BPT-LSL-TdTomato::Cd11c-yfp* mice, YFP and RFP were detected with 1020 nm excitation using the Yellow/Red (515–565 nm) filter, and second harmonics (collagen) were detected with 1020 nm excitation using the Blue/Green (460–500 nm) filters, separated by an LP 520 dichroic mirror. Overlapping images were assembled using the same acquisition software. For blood vessel tracing experiments using *BPT-LSL-TdTomato* mice, 950 nm excitation was used. FITC and second harmonics (collagen) was detected using the Blue/Green (460–500 nm) filter, and TdTomato was detected using the Green/Red (495–500 nm) filter, separated by an LP 570 dichroic mirror. We typically acquired 150-200 µm-deep Z-stacks with 4 µm

Species	*Gene*	*Primer Direction*	*Sequence 5′ - 3′*
Mouse	Gapdh	Forward	AACAGCAACTCCCACTCTTC
Mouse	Gapdh	Reverse	CCTGTT GCTGTAGCCGTATT
Mouse	Il1b	Forward	CGACAAAATACCTGTGGCCT
Mouse	Il1b	Reverse	TCTTCTTTGGGTATTGCTTGG
Mouse	Il6	Forward	CATGTTCTCTGGGAAATCGTGG
Mouse	Il6	Reverse	GTACTCCAGGTAGCTATGGTAC
Mouse	Vegfa	Forward	ATCTTCAAGCCGTCCTGTGTGC
Mouse	Vegfa	Reverse	TTTGACCCTTTCCCTTTCCTC
Mouse	Ang2	Forward	TTAGCACAAAGGATTCGGACAAT
Mouse	Ang2	Reverse	TTTTGTGGGTAGTACTGTCCATTCA
Mouse	Hif1a	Forward	ACCTTCATCGGAAACTCCAAAG
Mouse	Hif1a	Reverse	ACTGTTAGGCTCAGGTGAACT
Mouse	Tyrp1	Forward	AATGGAGAGTGGTCTGTGAATC
Mouse	Tyrp1	Reverse	CTGGGTTTCTCCTGATTGGTC

Table 1. **List of qRT-PCR Primers**

Z resolution, 12 tiles (4×3), with an X-Y resolution of 800 × 800 pixels per tile, and 0.6364 µm per pixel. Post-production processing of images was done using Fiji (v2.9.0), including tile stitching and quantification of GFP signal. FITC-Dextran Signal Area was calculated as the percentage of total GFP pixels above threshold in a maximum Z-projected image.

Immune Cell Isolation

Lymph nodes were mechanically disrupted and filtered through a 70-µm strainer to create single cell suspensions in cold complete RPMI (cRPMI) (RPMI 1640 media supplemented with 2 µM glutamine, 100 U/ml penicillin/streptomycin, and 10% FBS). Ears were mechanically dissociated and then digested in 100 µg/mL Liberase, 500 µg/mL Hyaluronidase, 10 mM HEPES, in up to 5 mL serum-free DMEM, incubated for 1 hour at 37°C, and filtered over 70 µm nylon mesh to create single cell suspensions in cold cRPMI. Isolated B16F10 tumors were mechanically dissociated and then digested in 1 mg/mL Collagenase III for 1 hour at 37°C, and then filtered through a 70-µm strainer. Tumor homogenate was then centrifuged over a 40/80% Percoll gradient to isolate immune cells.

Intracellular cytokine and transcription factor staining

Intracellular cytokine staining was performed using the Cytofix/Cytoperm PlusKit per manufacturer's instructions. In brief, single-cell suspensions from freshly harvested dLN were stimulated with PMA (20 ng/mL) and ionomycin (1 µg/mL) for 4 hours at 37 °C in the presence of GolgiPlug (brefeldin A). After staining for cell-surface molecules, the cells were fixed, permeabilized, and stained with antibodies to IFNγ, IL-17a, and IL-4. Flow cytometry antibodies are listed in Table 2.

Flow cytometry

Single cell suspensions were washed and resuspended with FACS buffer (PBS, 2% FBS, 0.02% Sodium Azide) containing purified rat anti-mouse CD16/CD32 (Fc Block). Cells were then stained with antibody cocktails for 20 minutes at 4°C. When necessary, intracellular Foxp3 staining was performed using a Foxp3 mouse T_{reg} cell staining kit (eBioscience). Cells were washed with FACS buffer after staining, resuspended in FACS buffer, and analyzed using a Cytek Biosciences Aurora Flow Cytometer. Flow cytometry data was analyzed with FlowJo (v10.0) software (BD Biosciences).

Quantification and statistical analysis

Unless otherwise stated, data in graphs are shown as mean ± standard deviation (SD). Statistical analyses were performed using Prism 10 (GraphPad v10.1.1). Statistical tests (e.g. one-way ANOVA, paired t-test, etc.), sample size (n) and what n represents (e.g. number of mice) are documented in the figure legends.

Single-Cell RNA Sequencing

Single-cell RNA sequencing was performed on FACS-sorted cell populations using the Chromium instrument (10x Genomics) following the manufacturer's protocol for 3' v3 chemistry. Briefly, single-cell suspensions were washed and resuspended in FACS buffer containing antibodies against rat anti-mouse CD45 and/or rat anti-mouse Ly6G, followed by staining for 30 minutes at 4°C. Cells were then washed, resuspended in FACS buffer, and sorted using an Aria II cytometer (BD Biosciences). Sorted cells were subsequently stained with TotalSeqTM-B barcoded hashing antibodies for sample multiplexing (Table 2). Immune cells from each condition were pooled at equal ratios, washed twice with PBS containing 0.05% bovine serum albumin (BSA), and resuspended in PBS with 0.04% BSA to a final concentration of 700–1,300 cells per µL. Cell viability was confirmed to be above 70% using 0.2% (w/v) Trypan Blue staining (Countess II). Library preparation of single-cell suspensions containing hash-tagged cells was performed by the MSKCC Integrated Genomics Operation (IGO) Core Facility. Subsequent cell capture, reverse transcription, cDNA amplification, and library construction were carried out according to the standard 10x Genomics protocol. Raw sequencing data were processed using the 10x Genomics

Receptor	Conjugate	Clone	Manufacturer	Catalog #	Purpose
B220(CD45R)	RA3-6B2	BV570	Biolegend	103237	Flow Cytometry
CCR2	SA203G11	BV650	Biolegend	150613	Flow Cytometry
CD103	2E7	PB	Biolegend	121417	Flow Cytometry
CD115 (CSF1R)	AFS98	APC	Biolegend	135509	Flow Cytometry
CD11b	M1/70	APC-Cy7	Tonbo Biosciences	25-0112- U100	Flow Cytometry
CD11b	M1/70	PE-CY7	eBioscience	25-0112-81	Flow Cytometry
CD16/CD32	2.4G2		Tonbo Biosciences	70-0161- M001	Flow Cytometry
CD19	1D3	BUV737	BD Biosciences	612782	Flow Cytometry
CD19	1D3	FITC	Biolegend	152403	Flow Cytometry
CD25	PC61	BV510	Biolegend	102041	Flow Cytometry
CD3	17A2	RF710	Tonbo Biosciences	80-0032-U100	Flow Cytometry

Table 2. **List of Antibodies**

CD4	BUV395	GK1.5	BD Biosciences	563790	Flow Cytometry
CD4	RM4-5	PE-Cy7	Tonbo Biosciences	60-0042- U100	Flow Cytometry
CD40	3/23	PB	Biolegend	124625	Flow Cytometry
CD44	IM7	BV650	Biolegend	103049	Flow Cytometry
CD45	30-F11	BV510	Biolegend	103138	Flow Cytometry
CD45	30-F11	BV605	BD Biosciences	563053	Flow Cytometry
CD45	30-F11	PerCP Cy5.5	Biolegend	103131	Flow Cytometry
CD45.2	104	BV605	Biolegend	109841	Flow Cytometry
CD62L	MEL-14	APC-CY7	Biolegend	104427	Flow Cytometry
CD8a	53-6.7	BUV805	BD Biosciences	612898	Flow Cytometry
CTLA4 (CD152)	UC10-4B9	APC	eBioscience	17-1522-82	Flow Cytometry
CX3CR1	SA011F11	BV785	Biolegend	149029	FlowCytometry
EpCAM (CD326)	G8.8	BUV395	BD Biosciences	740281	Flow Cytometry
F4/80	BM8	APC-Cy7	Biolegend	123117	Flow Cytometry
Foxp3	FJK-16s	eFluor 450	Thermo Fisher Scientific	48-5773-82	Flow Cytometry
GATA-3	AF647	L50-823	BD Biosciences	560069	Flow Cytometry
ICOS	C398.4A	BV785	Biolegend	313534	Flow Cytometry
IFNG	ef450	XMG1.2	Invitrogen	48-7311-82	Flow Cytometry
IL-17a	BV711	eBio17B7	Invitrogen	407-7177-82	Flow Cytometry
IL-4	PE-Cy7	BVD6-24G2	eBioscience	25-7042-82	Flow Cytometry
Lag3	C9B7W	BV711	Biolegend	125243	Flow Cytometry
Ly6C	HK1.4	BV711	Biolegend	128037	Flow Cytometry
LY6G	1A8	FITC	Biolegend	127605	Flow Cytometry
MHCII (I- A/I-E)	M5/114.15.2	AF700	eBioscience	56-5321-80	Flow Cytometry
NK1.1	PK136	FITC	Biolegend	108705	Flow Cytometry
PD-1	RMP1-30	PerCP Cy5.5	Biolegend	109120	Flow Cytometry
RORGT	BV786	Q31-378	BD Biosciences	564723	Flow Cytometry
Tbet	AF488	04-46	BD Biosciences	561266	Flow Cytometry
TCRb	H57597	FITC	Biolegend	109205	Flow Cytometry
H-2/CD45	301	M1/42; 30-F11	Biolegend	155831	TotalSeq-B Hashing
H-2/CD45	302	M1/42; 30-F11	Biolegend	155833	TotalSeq-B Hashing
H-2/CD45	303	M1/42; 30-F11	Biolegend	155835	TotalSeq-B Hashing
H-2/CD45	304	M1/42; 30-F11	Biolegend	155837	TotalSeq-B Hashing

Table 2. (continued)

H-2/CD45	305	M1/42; 30-F11	Biolegend	155839	TotalSeq-B Hashing
H-2/CD45	306	M1/42; 30-F11	Biolegend	155841	TotalSeq-B Hashing
H-2/CD45	307	M1/42; 30-F11	Biolegend	155843	TotalSeq-B Hashing
H-2/CD45	308	M1/42; 30-F11	Biolegend	155845	TotalSeq-B Hashing
H-2/CD45	309	M1/42; 30-F11	Biolegend	155847	TotalSeq-B Hashing
H-2/CD45	310	M1/42; 30-F11	Biolegend	155849	TotalSeq-B Hashing

Table 2. (continued)

Cell Ranger pipeline. The Cell Ranger mkfastq tool was used to demultiplex raw sequencing files (BCL format) into FASTQ files. Alignment of gene expression libraries to the GRCm39 reference transcriptome, generation of count matrices, and processing of feature barcode and VDJ library reads, were performed using the Cell Ranger (v9.0) default pipeline. For downstream analysis, the Seurat package (v5.2.0) in R (v4.2.3) was used. Data from all scRNA-seq samples were merged into a single aggregated Seurat object using IntegrateData()[76]. Hashtags were demultiplexed using HTODemux()[77]. The standard Seurat workflow was followed, including quality control, normalization, feature selection, dimensionality reduction, clustering, and differential expression analysis. Immune cell subsets were annotated against the Immgen database using the SingleR R package[78]. Cell lineage trajectories and pseudotime values were inferred using Slingshot[79].

Figure supplements

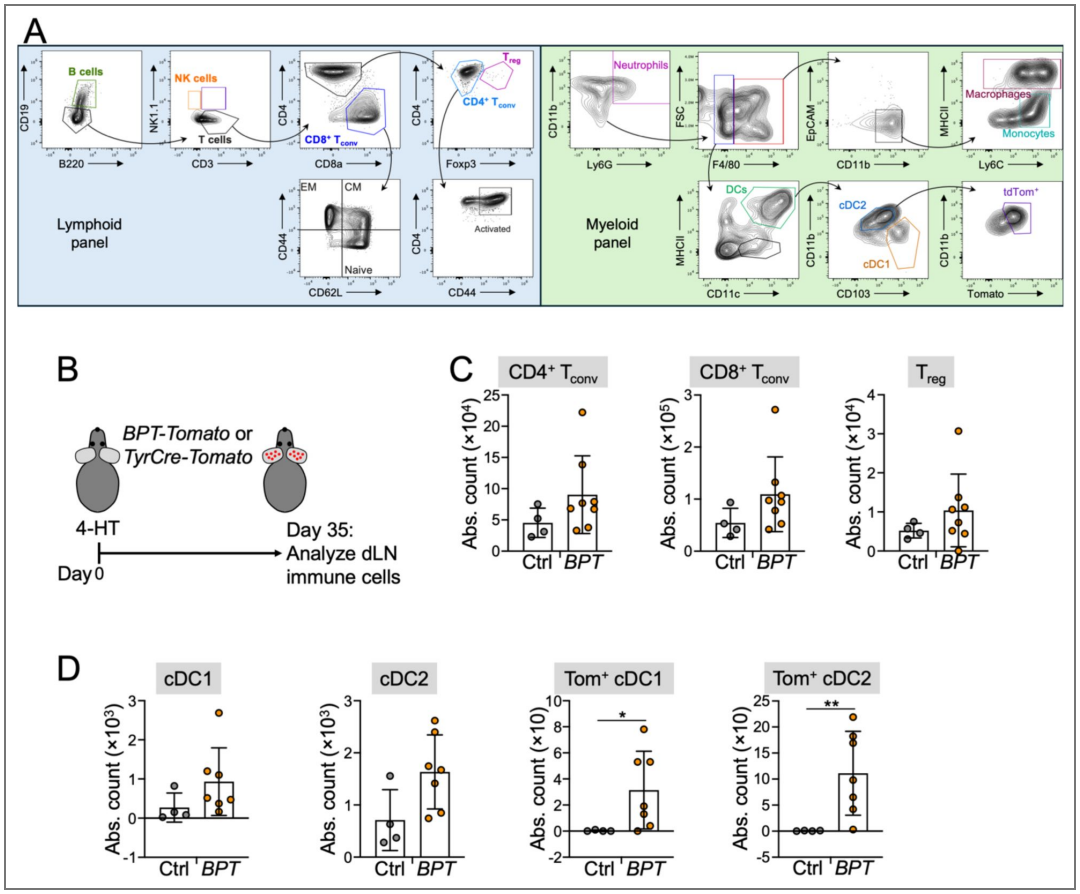

Figure 1- figure supplement 1. Flow cytometric analysis of *BPT* mice. (A) Gating strategies for lymphoid (left) and myeloid (right) panels, starting from live, CD45$^+$ singlets. (B-C) *BPT-TdTomato* and *Tyr-TdTomato* control mice were 4-HT-painted and CD45$^+$ cells in the dLN enumerated after 35 days by flow cytometry. (B) Schematic diagram of the experimental approach. (C) Quantification of the indicated T cell subsets. (D) Quantification of the indicated myeloid cell subsets. Tom$^+$ = TdTomato positive. * and ** denote P ≤ 0.05 and P < 0.01, respectively, calculated by Mann-Whitney test.

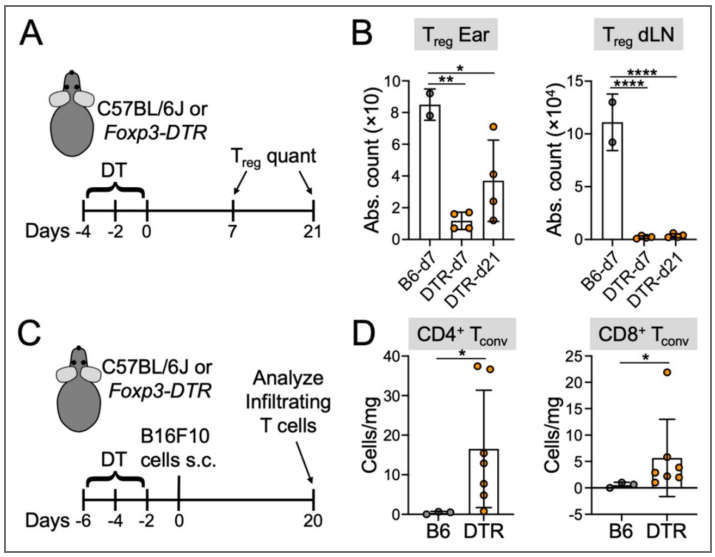

Figure 2 - supplement 1. Flow cytometric analysis of T_{reg} cell depletion and T_{conv} cell infiltration in *Foxp3-DTR* mice.

(A-B) *Foxp3-DTR* mice and C57BL/6J controls were DT-treated and T_{reg} cells quantified by flow cytometry in the ear skin and dLN 7 and 21 days after the last DT dose. (A) Schematic diagram of the experimental approach. (B) Absolute count of T_{reg} cells in the ear skin (left) and dLN (right). Error bars indicate SD. *, **, and **** denote $P \leq 0.05$, $P < 0.01$, and $P < 0.0001$, respectively, calculated by one-way ANOVA. N = 2 C57BL/6J control mice and 4 *Foxp3-DTR* mice. (C-D) *Foxp3-DTR* mice and C57BL/6J controls were DT-treated and then injected s.c. with B16F10 cells. 20 days later, tumor infiltrating T cells were quantified by flow cytometry. (C) Schematic diagram of the experimental approach. (D) Quantification of tumor infiltrating $CD4^+$ (left) and $CD8^+$ (right) T_{conv} cells. Error bars indicate SD. * denotes $P \leq 0.05$, calculated by lognormal Welch's t-test. N = 3 C57BL/6J control mice and 7 *Foxp3-DTR* mice.

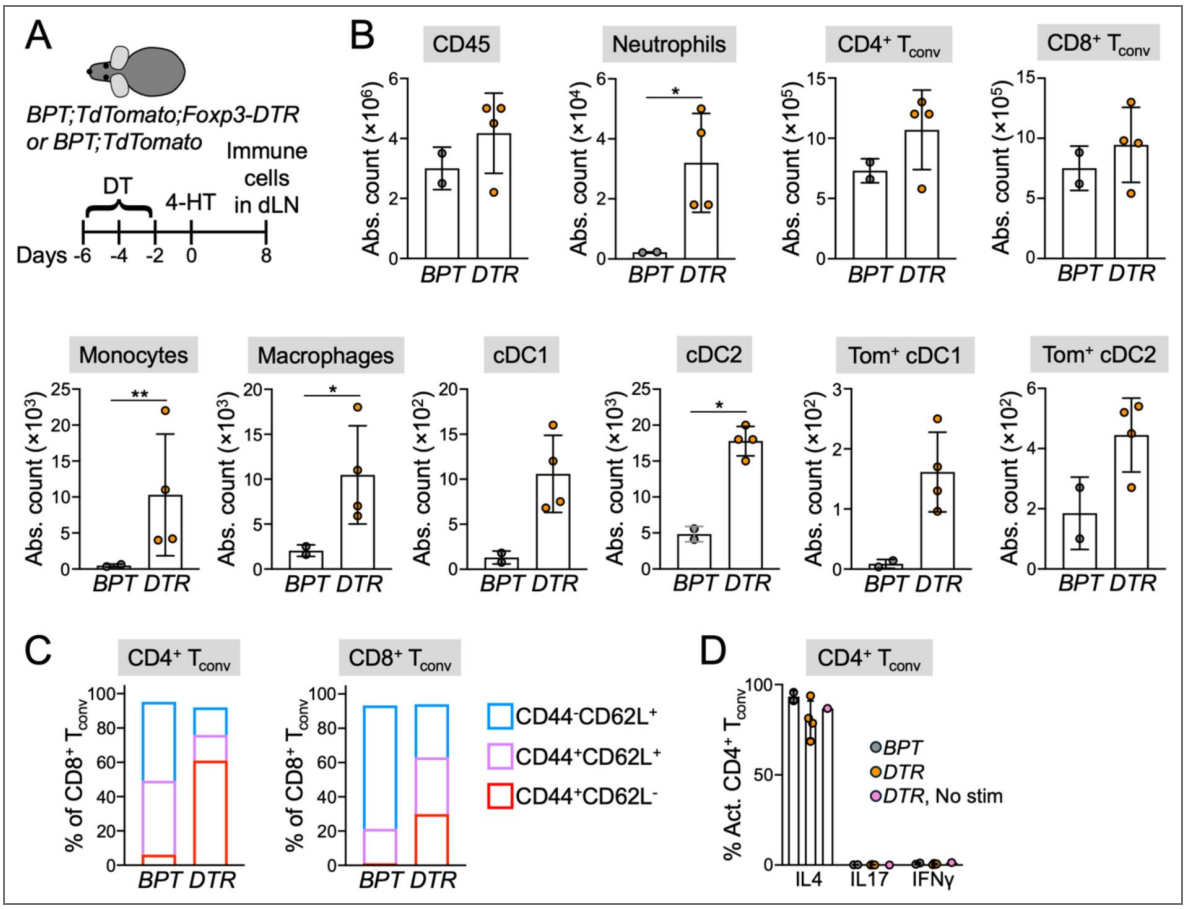

Figure 3 - supplement 1. **T_{reg} cell depletion drives multimodal inflammation in the dLN.**

BPT-TdTomato;Foxp3-DTR mice and *BPT-TdTomato* controls were treated with DT, followed by 4-HT painting, and immune cells in the dLN enumerated by flow cytometry after 8 days. (A) Schematic of the experimental protocol. (B) Quantification of the indicated immune cell subsets. Tom^+ = TdTomato positive. * and ** denote $P \leq 0.05$ and $P < 0.01$, respectively, calculated by lognormal Welch's t-test. N = 2 *BPT-TdTomato* mice and 4 *BPT-TdTomato;Foxp3-DTR* mice. (C) Subset analysis of $CD4^+$ (left) and $CD8^+$ (right) T_{conv} cells in the dLN at the experimental endpoint. Fractions of total represent mean values derived from N = 2 *BPT* mice and N = 4 *BPT;Foxp3-DTR* mice. (D) Intracellular cytokine staining by $CD4^+$ T_{conv} cells after *in vitro* stimulation with PMA/ionomycin. Error bars indicate SD. N = 2 *BPT* mice and N = 4 *BPT;Foxp3-DTR* mice.

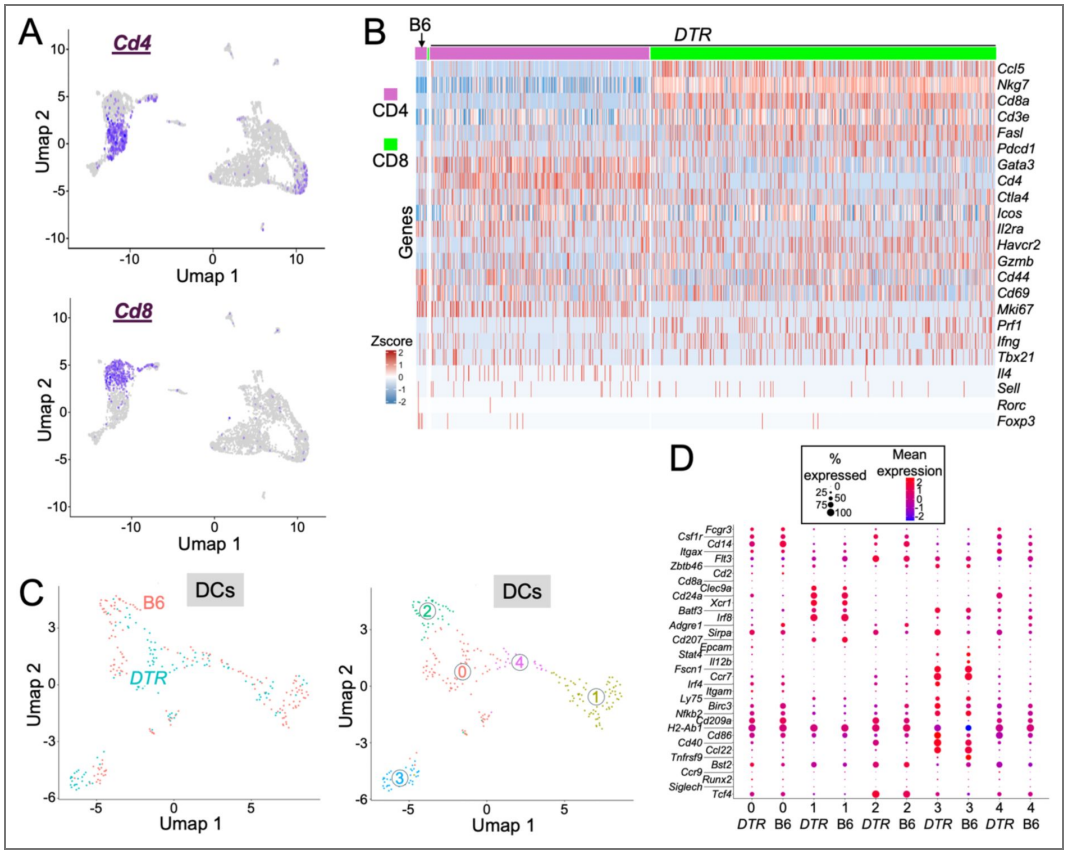

Figure 4 - supplement 1. **T_{reg} cell depletion drives multimodal inflammation in the skin.**

$CD45^{+}$cells extracted from the ear skin of *Foxp3-DTR* mice or C57BL/6J controls were analyzed by scRNA-seq 8 days after DT treatment. (A) Feature plots of the all cell UMAP, showing expression of *Cd4* and *Cd8*. (B) Gene expression heat map of Immgen-defined T cells, organized by sample (CD57BL/6J (B6) or *Foxp3-DTR* (DTR)) and by lineage (CD4 or CD8). (C) UMAP reclustering of the DCs identified in the all cell UMAP. Cells are colored by sample on the left and by Seurat cluster on the right. (D) Dot plot showing the expression of critical DC lineage genes, organized by sample and Seurat cluster.

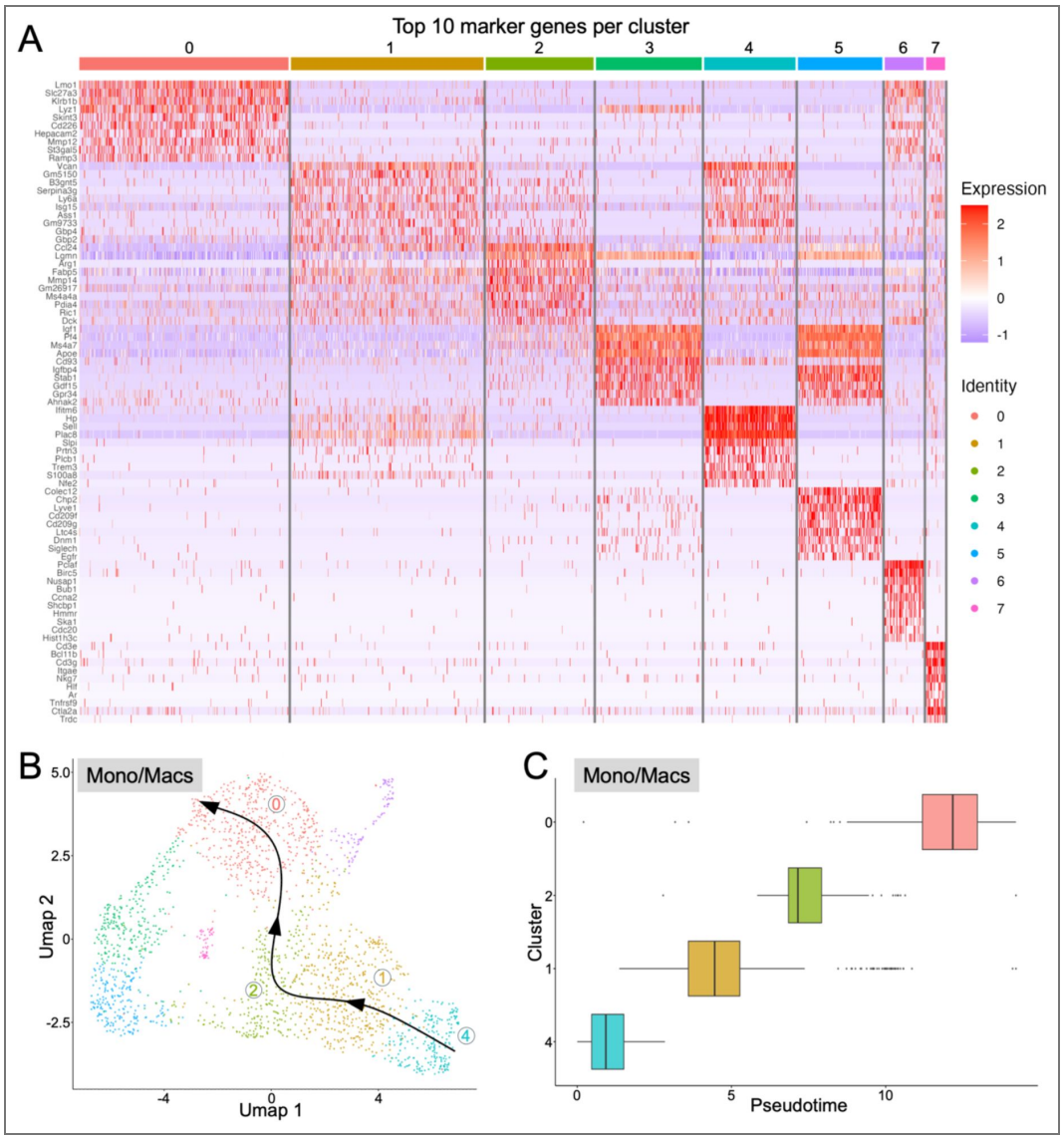

Figure 4 - supplement 2. Inflammatory monocyte/macrophage recruitment and differentiation in T_{reg} cell-depleted skin.

CD45^{+} cells extracted from the ear skin of *Foxp3-DTR* mice or C57BL/6J controls were analyzed by scRNA-seq 8 days after DT treatment. Monocyte and macrophage clusters from the all cell analysis were subjected to Seurat reclustering. (A) Heat map showing the differentially expressed genes that define the resulting monocyte/macrophage clusters. (B-C) Pseudotime analysis was performed on clusters 0, 1, 2, and 4. (B) Pseudotime trajectory output mapped onto the monocyte/macrophage UMAP. (C) The pseudotime distribution of each cluster, with central line denoting median, colored boxes denoting the central 50th percentile, and whiskers indicating the range, with outliers (determined by Tukey's method) shown as individual dots.

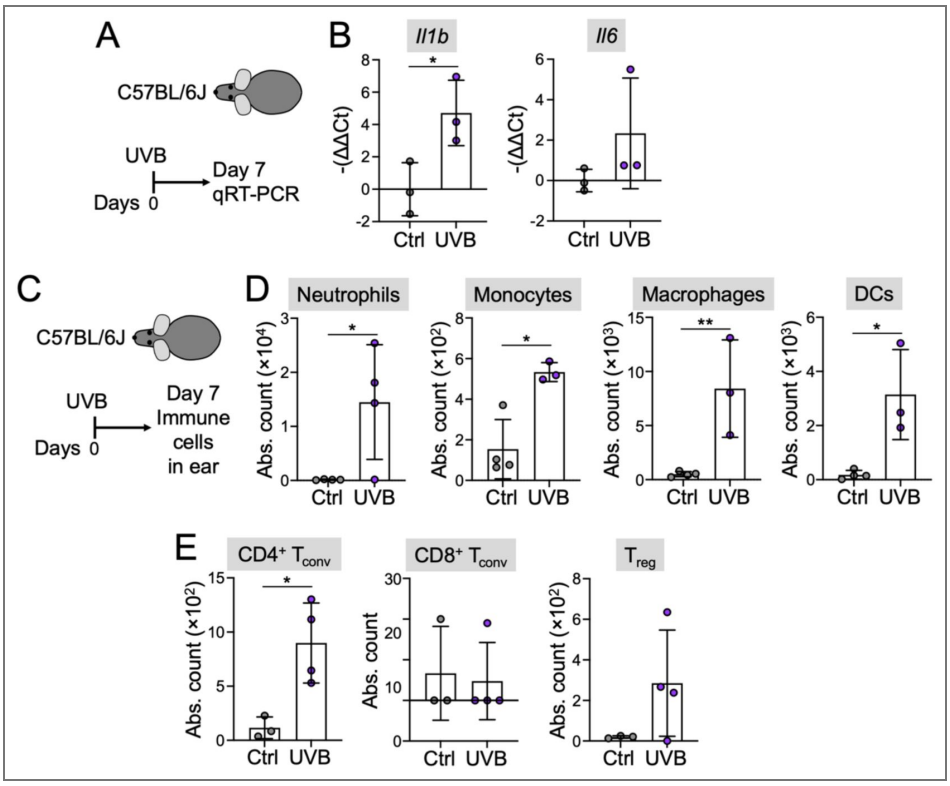

Figure 6 - supplement 1. UVB induces cutaneous inflammation.

(A-B) C57BL/6J mice were UVB- or mock-irradiated and qRT-PCR performed on skin homogenates 7 days later. (A) Schematic of the experimental protocol. (B) Quantified expression of the indicated genes. * denotes $P \leq 0.05$, calculated by unpaired t-test. $N \geq 3$ mice per group. (C-E) C57BL/6J mice were UVB- or mock-irradiated and immune cells in the ear skin enumerated by flow cytometry after 8 days. (C) Schematic of the experimental protocol. (D) Quantification of the indicated myeloid cell subsets. (E) Quantification of the indicated T cell subsets. In D and E, error bars indicate SD. * and ** denote $P \leq 0.05$ and $P < 0.01$, respectively, calculated by lognormal Welch's t-test. $N \geq 3$ mice per group.

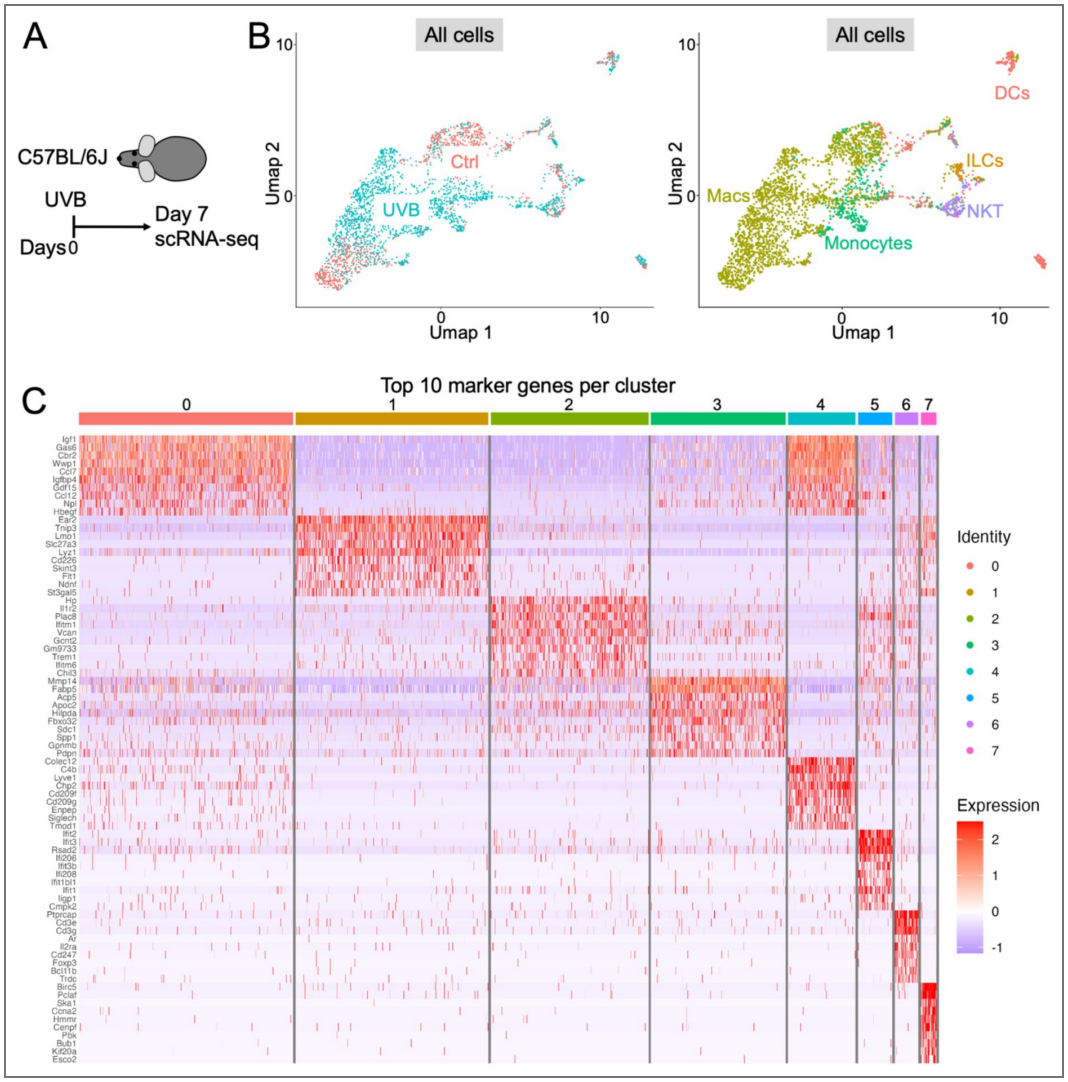

Figure 6 - supplement 2. UVB irradiation drives multimodal inflammation in the skin.

C57BL/6J mice were exposed to UVB or mock irradiation and CD45^{+} cells from the ear skin analyzed by scRNA-seq 7 days later. (A) Schematic of the experimental protocol. (B) UMAP showing all sequenced cells from both samples, colored by sample on the left and by cell type on the right. (C) Monocyte and macrophage clusters from the all cell analysis were subjected to Seurat reclustering. The heat map shows differentially expressed genes that define the resulting monocyte/macrophage clusters.

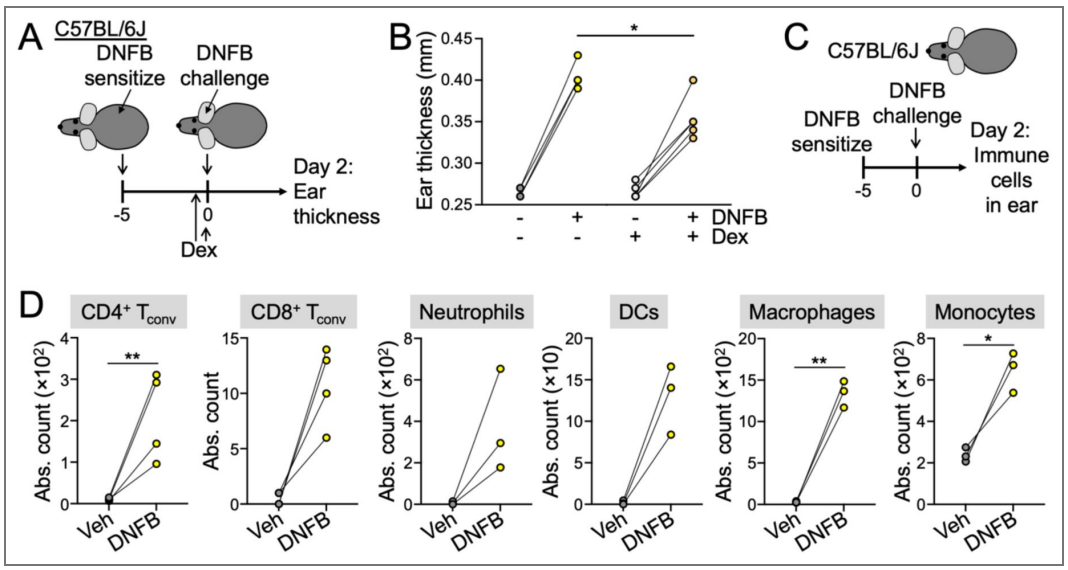

Figure 7 - supplement 1. DNFB-induced hypersensitivity drives cutaneous inflammation.

(A-B) C57BL/6J mice were sensitized with DNFB and then rechallenged on one ear in the presence or absence of Dex therapy. Ear thickness was measured 2 days after elicitation. (A) Schematic of the experimental protocol. (B) Ear thickness measurements, pairing DNFB-elicited ears with contralateral controls. N = 4 mice per group. * denotes $P \leq 0.05$, calculated by unpaired t-test. (C-D) C57BL/6J mice were sensitized with DNFB and then rechallenged 5 days later. Immune cells in the ear were enumerated by flow cytometry 2 days after elicitation. (C) Schematic of the experimental protocol. (D) Infiltration of the indicated immune subsets, pairing DNFB-elicited ears with contralateral controls. N = 4 mice per group. * and ** denote $P \leq 0.05$ and $P < 0.01$, respectively, calculated by paired lognormal t-test.

Data availability

scRNA-seq data will be deposited in GEO. Code will deposited with github. All other source data will be available upon request.

Acknowledgements

We thank A. Y. Rudensky, J. Wolchok, and T. Merghoub for mice; A. Schietinger and M. O. Li for conceptual guidance; G. Diehl for critical reading of the manuscript; the MSKCC Flow Cytometry Core Facility for FACS purification; the MSKCC Integrated Genomics Operation for library preparation and sequencing; and members of the M. Huse lab for advice. Supported in part by the US National Institutes of Health (R01-AI087644 to M. H., R01-CA286566 to M. H., R01-AR077664 to J. H. Z., F31-CA294974 to Y. A. E., P30-CA008748 to MSKCC), the Ludwig Center for Cancer Immunotherapy (M. H.), the Vision of Children Foundation (J. H. Z.), and the National Organization for Albinism and Hypopigmentation (J. H. Z.).

Additional information

Funding

Funder	Grant reference number	Author
HHS | National Institutes of Health (NIH)	R01-AI087644	Morgan Huse
HHS | National Institutes of Health (NIH)	R01-CA286566	Morgan Huse
HHS | National Institutes of Health (NIH)	R01-AR077664	Jonathan H Zippin
HHS | National Institutes of Health (NIH)	F31-CA294974	Yassmin A Elbanna
HHS | National Institutes of Health (NIH)	P30-CA008748	Morgan Huse
Ludwig Center for Cancer Immunotherapy		Morgan Huse
Vision of Children Foundation (VOC)		Jonathan H Zippin
National Organization for Albinism and Hypopigmentation		Jonathan H Zippin

Author ORCID iDs

Jonathan H Zippin: https://orcid.org/0000-0002-5882-0189
Morgan Huse: https://orcid.org/0000-0001-9941-7719

References

1. **Didier AJ,** Nandwani SV, Watkins D, Fahoury AM, Campbell A, Craig DJ, Vijendra D, Parquet N (2024) Patterns and trends in melanoma mortality in the United States, 1999-2020. *BMC Cancer* **24**:790 https://doi.org/10.1186/s12885-024-12426-z | PubMed
2. **Switzer B,** Puzanov I, Skitzki JJ, Hamad L, Ernstoff MS (2022) Managing Metastatic Melanoma in 2022: A Clinical Review. *JCO Oncol Pract* **18**:335-351 https://doi.org/10.1200/OP.21.00686 | PubMed
3. **Leonardi GC,** Falzone L, Salemi R, Zanghi A, Spandidos DA, McCubrey JA, Candido S, Libra M (2018) Cutaneous melanoma: From pathogenesis to therapy (Review). *Int J Oncol* **52**:1071-1080 https://doi.org/10.3892/ijo.2018.4287 | PubMed
4. **Maverakis E,** Cornelius LA, Bowen GM, Phan T, Patel FB, Fitzmaurice S, He Y, Burrall B, Duong C, Kloxin AM, *et al.* (2015) Metastatic melanoma - a review of current and future treatment options. *Acta Derm Venereol* **95**:516-524 https://doi.org/10.2340/00015555-2035 | PubMed
5. **Pollock PM,** Harper UL, Hansen KS, Yudt LM, Stark M, Robbins CM, Moses TY, Hostetter G, Wagner U, Kakareka J, *et al.* (2003) High frequency of BRAF mutations in nevi. *Nat Genet* **33**:19-20 https://doi.org/10.1038/ng1054 | PubMed

6. **Hayward NK,** Wilmott JS, Waddell N, Johansson PA, Field MA, Nones K, Patch AM, Kakavand H, Alexandrov LB, Burke H, *et al.* (2017) Whole-genome landscapes of major melanoma subtypes. *Nature* **545**:175-180 https://doi.org/10.1038/nature22071 | PubMed

7. **Lozada JR,** Geyer FC, Selenica P, Brown D, Alemar B, Merghoub T, Berger MF, Busam KJ, Halpern AC, Weigelt B, *et al.* (2019) Massively parallel sequencing analysis of benign melanocytic naevi. *Histopathology* **75**:29-38 https://doi.org/10.1111/his.13843 | PubMed

8. **Gil-Barrachina M,** Hernando B, Perez-Pastor G, Alegre-de-Miquel V, Valenzuela-Onate C, Minguez-Lujan S, Monfort-Lanzas P, Tomas-Bort E, Marques-Torrejon MA, Martinez-Cadenas C (2026) Genetic Evolution of Melanoma: Comparative Analysis of Candidate Gene Mutations in Healthy Skin, Nevi, and Tumors from the Same Patients. *Int J Mol Sci* **27** https://doi.org/10.3390/ijms27010532 | PubMed

9. **Lee KJ,** Kao YC, Jiang A, Prokofyeva A, Tom LN, Jagirdar K, Smit DJ, Oey HM, Tan JM, Ainger SA, *et al.* (2026) Subclinical fields of BRAF V600E-mutant melanocytes populate human skin and are enriched around melanoma and naevi. *Br J Dermatol* **194**:301-310 https://doi.org/10.1093/bjd/ljaf412 | PubMed

10. **Maher NG,** Scolyer RA, Colebatch AJ (2023) Biology and genetics of acquired and congenital melanocytic naevi. *Pathology* **55**:169-177 https://doi.org/10.1016/j.pathol.2022.12.344 | PubMed

11. **Schreiber RD,** Old LJ, Smyth MJ (2011) Cancer immunoediting: integrating immunity's roles in cancer suppression and promotion. *Science* **331**:1565-1570 https://doi.org/10.1126/science.1203486 | PubMed

12. **Shalapour S,** Karin M (2015) Immunity, inflammation, and cancer: an eternal fight between good and evil. *J Clin Invest* **125**:3347-3355 https://doi.org/10.1172/JCI80007 | PubMed

13. **Postow MA,** Callahan MK, Wolchok JD (2015) Immune Checkpoint Blockade in Cancer Therapy. *J Clin Oncol* **33**:1974-1982 https://doi.org/10.1200/JCO.2014.59.4358 | PubMed

14. **Wei SC,** Duffy CR, Allison JP (2018) Fundamental Mechanisms of Immune Checkpoint Blockade Therapy. *Cancer Discov* **8**:1069-1086 https://doi.org/10.1158/2159-8290.CD-18-0367 | PubMed

15. **Josefowicz SZ,** Lu LF, Rudensky AY (2012) Regulatory T cells: mechanisms of differentiation and function. *Annu Rev Immunol* **30**:531-564 https://doi.org/10.1146/annurev.immunol.25.022106.141623 | PubMed

16. **Bos PD,** Plitas G, Rudra D, Lee SY, Rudensky AY (2013) Transient regulatory T cell ablation deters oncogene-driven breast cancer and enhances radiotherapy. *J Exp Med* **210**:2435-2466 https://doi.org/10.1084/jem.20130762 | PubMed

17. **Shabaneh TB,** Molodtsov AK, Steinberg SM, Zhang P, Torres GM, Mohamed GA, Boni A, Curiel TJ, Angeles CV, Turk MJ (2018) Oncogenic BRAF(V600E) Governs Regulatory T-cell Recruitment during Melanoma Tumorigenesis. *Cancer Res* **78**:5038-5049 https://doi.org/10.1158/0008-5472.CAN-18-0365 | PubMed

18. **Binnewies M,** Mujal AM, Pollack JL, Combes AJ, Hardison EA, Barry KC, Tsui J, Ruhland MK, Kersten K, Abushawish MA, *et al.* (2019) Unleashing Type-2 Dendritic Cells to Drive Protective Antitumor CD4(+) T Cell Immunity. *Cell* **177**:556-571.e516. https://doi.org/10.1016/j.cell.2019.02.005 | PubMed

19. **Klages K,** Mayer CT, Lahl K, Loddenkemper C, Teng MWL, Ngiow SF, Smyth MJ, Hamann A, Huehn J, Sparwasser T (2010) Selective Depletion of Foxp3(+) Regulatory T Cells Improves Effective Therapeutic Vaccination against Established Melanoma. *Cancer Research* **70**:7788-7799 https://doi.org/10.1158/0008-5472.Can-10-1736 | PubMed

20. **Hanahan D** (2026) Hallmarks of cancer-Then and now, and beyond. *Cell* **189**:2254-2277 https://doi.org/10.1016/j.cell.2025.12.049 | PubMed

21. **Ortega-Gomez A,** Perretti M, Soehnlein O (2013) Resolution of inflammation: an integrated view. *EMBO Mol Med* **5**:661-674 https://doi.org/10.1002/emmm.201202382 | PubMed

22. **Rivera LB,** Bergers G (2015) Intertwined regulation of angiogenesis and immunity by myeloid cells. *Trends Immunol* **36**:240-249 https://doi.org/10.1016/j.it.2015.02.005 | PubMed

23. **De Palma M,** Biziato D, Petrova TV (2017) Microenvironmental regulation of tumour angiogenesis. *Nat Rev Cancer* **17**:457-474 https://doi.org/10.1038/nrc.2017.51 | PubMed

24. **Bernard JJ,** Gallo RL, Krutmann J (2019) Photoimmunology: how ultraviolet radiation affects the immune system. *Nat Rev Immunol* **19**:688-701 https://doi.org/10.1038/s41577-019-0185-9 | PubMed

25. **Schwarz T** (2010) The dark and the sunny sides of UVR-induced immunosuppression: photoimmunology revisited. *J Invest Dermatol* **130**:49-54 https://doi.org/10.1038/jid.2009.217 | PubMed

26. **Clydesdale GJ,** Dandie GW, Muller HK (2001) Ultraviolet light induced injury: immunological and inflammatory effects. *Immunol Cell Biol* **79**:547-568 https://doi.org/10.1046/j.1440-1711.2001.01047.x | PubMed

27. **Alexandrov LB,** Nik-Zainal S, Wedge DC, Aparicio SA, Behjati S, Biankin AV, Bignell GR, Bolli N, Borg A, Borresen-Dale AL, *et al.* (2013) Signatures of mutational processes in human cancer. *Nature* **500**:415-421 https://doi.org/10.1038/nature12477 | PubMed

28. **Viros A,** Sanchez-Laorden B, Pedersen M, Furney SJ, Rae J, Hogan K, Ejiama S, Girotti MR, Cook M, Dhomen N, *et al.* (2014) Ultraviolet radiation accelerates BRAF-driven melanomagenesis by targeting TP53. *Nature* **511**:478-482 https://doi.org/10.1038/nature13298 | PubMed

29. **Hodis E,** Watson IR, Kryukov GV, Arold ST, Imielinski M, Theurillat JP, Nickerson E, Auclair D, Li L, Place C, *et al.* (2012) A landscape of driver mutations in melanoma. *Cell* **150**:251-263 https://doi.org/10.1016/j.cell.2012.06.024 | PubMed

30. **Shain AH,** Joseph NM, Yu R, Benhamida J, Liu S, Prow T, Ruben B, North J, Pincus L, Yeh I, *et al.* (2018) Genomic and Transcriptomic Analysis Reveals Incremental Disruption of Key Signaling Pathways during Melanoma Evolution. *Cancer Cell* **34**:45-55.e44. https://doi.org/10.1016/j.ccell.2018.06.005 | PubMed

31. **Muller HK,** Malley RC, McGee HM, Scott DK, Wozniak T, Woods GM (2008) Effect of UV radiation on the neonatal skin immune system- implications for melanoma. *Photochem Photobiol* **84**:47-54 https://doi.org/10.1111/j.1751-1097.2007.00246.x | PubMed

32. **Mo X,** Preston S, Zaidi MR (2019) Macroenvironment-gene-microenvironment interactions in ultraviolet radiation-induced melanomagenesis. *Adv Cancer Res* **144**:1-54 https://doi.org/10.1016/bs.acr.2019.03.008 | PubMed

33. **Sample A,** He YY (2018) Mechanisms and prevention of UV-induced melanoma. *Photodermatol Photoimmunol Photomed* **34**:13-24 https://doi.org/10.1111/phpp.12329 | PubMed

34. **Gieniusz E,** Skrzydlewska E, Luczaj W (2024) Current Insights into the Role of UV Radiation-Induced Oxidative Stress in Melanoma Pathogenesis. *Int J Mol Sci* **25** https://doi.org/10.3390/ijms252111651 | PubMed

35. **Enomoto A,** Yoshihisa Y, Yamakoshi T, Ur Rehman M, Norisugi O, Hara H, Matsunaga K, Makino T, Nishihira J, Shimizu T (2011) UV-B radiation induces macrophage migration inhibitory factor-mediated melanogenesis through activation of protease-activated receptor-2 and stem cell factor in keratinocytes. *Am J Pathol* **178**:679-687 https://doi.org/10.1016/j.ajpath.2010.10.021 | PubMed

36. **Mukhopadhyay P,** Ferguson B, Muller HK, Handoko HY, Walker GJ (2016) Murine melanomas accelerated by a single UVR exposure carry photoproduct footprints but lack UV signature C>T mutations in critical genes. *Oncogene* **35**:3342-3350 https://doi.org/10.1038/onc.2015.386 | PubMed

37. **Bowman RL,** Hennessey RC, Weiss TJ, Tallman DA, Crawford ER, Murphy BM, Webb A, Zhang S, La Perle KM, Burd CJ, *et al.* (2021) UVB mutagenesis differs in Nras- and Braf-mutant mouse models of melanoma. *Life Sci Alliance* **4** https://doi.org/10.26508/lsa.202101135 | PubMed

38. **Gandini S,** Sera F, Cattaruzza MS, Pasquini P, Picconi O, Boyle P, Melchi CF (2005) Meta-analysis of risk factors for cutaneous melanoma: II. Sun exposure. *Eur J Cancer* **41**:45-60 https://doi.org/10.1016/j.ejca.2004.10.016 | PubMed

39. **Weiss TJ,** Crawford ER, Posada V, Rahman H, Liu T, Murphy BM, Arnold TE, Gray S, Hu Z, Hennessey RC, *et al.* (2023) Cell-intrinsic melanin fails to protect melanocytes from ultraviolet-mutagenesis in the absence of epidermal melanin. *Pigment Cell Melanoma Res* **36**:6-18 https://doi.org/10.1111/pcmr.13070 | PubMed

40. **Hennessey RC,** Holderbaum AM, Bonilla A, Delaney C, Gillahan JE, Tober KL, Oberyszyn TM, Zippin JH, Burd CE (2017) Ultraviolet radiation accelerates NRas-mutant melanomagenesis: A cooperative effect blocked by sunscreen. *Pigment Cell Melanoma Res* **30**:477-487 https://doi.org/10.1111/pcmr.12601 | PubMed

41. **An HT,** Yoo JY, Lee MK, Shin MH, Rhie GE, Seo JY, Chung JH, Eun HC, Cho KH (2001) Single dose radiation is more effective for the UV-induced activation and proliferation of melanocytes than fractionated dose radiation. *Photodermatol Photoimmunol Photomed* **17**:266-271 https://doi.org/10.1034/j.1600-0781.2001.170604.x | PubMed

42. **Yamazaki S,** Nishioka A, Kasuya S, Ohkura N, Hemmi H, Kaisho T, Taguchi O, Sakaguchi S, Morita A (2014) Homeostasis of thymus-derived Foxp3+ regulatory T cells is controlled by ultraviolet B exposure in the skin. *J Immunol* **193**:5488-5497 https://doi.org/10.4049/jimmunol.1400985 | PubMed

43. **Yamazaki S,** Odanaka M, Nishioka A, Kasuya S, Shime H, Hemmi H, Imai M, Riethmacher D, Kaisho T, Ohkura N, *et al.* (2018) Ultraviolet B-Induced Maturation of CD11b-Type Langerin(-) Dendritic Cells Controls the Expansion of Foxp3(+) Regulatory T Cells in the Skin. *J Immunol* **200**:119-129 https://doi.org/10.4049/jimmunol.1701056 | PubMed

44. **Hesterberg RS,** Amorrortu RP, Zhao Y, Hampras S, Akuffo AA, Fenske N, Cherpelis B, Balliu J, Vijayan L, Epling-Burnette PK, *et al.* (2018) T Regulatory Cell Subpopulations Associated with Recent Ultraviolet Radiation Exposure in a Skin Cancer Screening Cohort. *J Immunol* **201**:3269-3281 https://doi.org/10.4049/jimmunol.1800940 | PubMed

45. **Dankort D,** Curley DP, Cartlidge RA, Nelson B, Karnezis AN, Damsky WE, You MJ, DePinho RA, McMahon M, Bosenberg M (2009) Braf(V600E) cooperates with Pten loss to induce metastatic melanoma. *Nature Genetics* **41**:544-552 https://doi.org/10.1038/ng.356 | PubMed

46. **Roberts EW,** Broz ML, Binnewies M, Headley MB, Nelson AE, Wolf DM, Kaisho T, Bogunovic D, Bhardwaj N, Krummel MF (2016) Critical Role for CD103(+)/CD141(+) Dendritic Cells Bearing CCR7 for Tumor Antigen Trafficking and Priming of T Cell Immunity in Melanoma. *Cancer Cell* **30**:324-336 https://doi.org/10.1016/j.ccell.2016.06.003 | PubMed

47. **Kim JM,** Rasmussen JP, Rudensky AY (2007) Regulatory T cells prevent catastrophic autoimmunity throughout the lifespan of mice. *Nat Immunol* **8**:191-197 https://doi.org/10.1038/ni1428 | PubMed

48. **Boothby IC,** Kinet MJ, Boda DP, Kwan EY, Clancy S, Cohen JN, Habrylo I, Lowe MM, Pauli M, Yates AE, *et al.* (2021) Early-life inflammation primes a T helper 2 cell-fibroblast niche in skin. *Nature* **599**:667-672 https://doi.org/10.1038/s41586-021-04044-7 | PubMed

49. **Bieber K,** Sun S, Witte M, Kasprick A, Beltsiou F, Behnen M, Laskay T, Schulze FS, Pipi E, Reichhelm N, *et al.* (2017) Regulatory T Cells Suppress Inflammation and Blistering in Pemphigoid Diseases. *Front Immunol* **8**:1628 https://doi.org/10.3389/fimmu.2017.01628 | PubMed

50. **Sontheimer C,** Liggitt D, Elkon KB (2017) Ultraviolet B Irradiation Causes Stimulator of Interferon Genes-Dependent Production of Protective Type I Interferon in Mouse Skin by Recruited Inflammatory Monocytes. *Arthritis Rheumatol* **69**:826-836 https://doi.org/10.1002/art.39987 | PubMed

51. **Toichi E,** Lu KQ, Swick AR, McCormick TS, Cooper KD (2008) Skin-infiltrating monocytes/macrophages migrate to draining lymph nodes and produce IL-10 after contact sensitizer exposure to UV-irradiated skin. *J Invest Dermatol* **128**:2705-2715 https://doi.org/10.1038/jid.2008.137 | PubMed

52. **Zhang AY,** Wu C, Zhou L, Ismail SA, Tao J, McCormick LL, Cooper KD, Gilliam AC (2006) Transduced monocyte/macrophages targeted to murine skin by UV light. *Exp Dermatol* **15**:51-57 https://doi.org/10.1111/j.0906-6705.2005.00394.x | PubMed

53. **Bernard JJ,** Cowing-Zitron C, Nakatsuji T, Muehleisen B, Muto J, Borkowski AW, Martinez L, Greidinger EL, Yu BD, Gallo RL (2012) Ultraviolet radiation damages self noncoding RNA and is detected by TLR3. *Nat Med* **18**:1286-1290 https://doi.org/10.1038/nm.2861 | PubMed

54. **Schwarz T,** Luger TA (1989) Effect of UV irradiation on epidermal cell cytokine production. *J Photochem Photobiol B* **4**:1-13 https://doi.org/10.1016/1011-1344(89)80097-1

55. **Yano K,** Kadoya K, Kajiya K, Hong YK, Detmar M (2005) Ultraviolet B irradiation of human skin induces an angiogenic switch that is mediated by upregulation of vascular endothelial growth factor and by downregulation of thrombospondin-1. *Br J Dermatol* **152**:115-121 https://doi.org/10.1111/j.1365-2133.2005.06368.x | PubMed

56. **Kim MS,** Kim YK, Eun HC, Cho KH, Chung JH (2006) All-trans retinoic acid antagonizes UV-induced VEGF production and angiogenesis via the inhibition of ERK activation in human skin keratinocytes. *J Invest Dermatol* **126**:2697-2706 https://doi.org/10.1038/sj.jid.5700463 | PubMed

57. **Di Nuzzo S,** Sylva-Steenland RM, de Rie MA, Das PK, Bos JD, Teunissen MB (1998) UVB radiation preferentially induces recruitment of memory CD4+ T cells in normal human skin: long-term effect after a single exposure. *J Invest Dermatol* **110**:978-981 https://doi.org/10.1046/j.1523-1747.1998.00220.x | PubMed

58. **Hatton JL,** Parent A, Tober KL, Hoppes T, Wulff BC, Duncan FJ, Kusewitt DF, VanBuskirk AM, Oberyszyn TM (2007) Depletion of CD4+ cells exacerbates the cutaneous response to acute and chronic UVB exposure. *J Invest Dermatol* **127**:1507-1515 https://doi.org/10.1038/sj.jid.5700746 | PubMed

59. **Schwarz A,** Philippsen R, Schwarz T (2023) Mouse Models of Allergic Contact Dermatitis: Practical Aspects. *J Invest Dermatol* **143**:888-892 https://doi.org/10.1016/j.jid.2023.03.1668 | PubMed

60. **Fyhrquist N,** Lehtimaki S, Lahl K, Savinko T, Lappetelainen AM, Sparwasser T, Wolff H, Lauerma A, Alenius H (2012) Foxp3+ cells control Th2 responses in a murine model of atopic dermatitis. *J Invest Dermatol* **132**:1672-1680 https://doi.org/10.1038/jid.2012.40 | PubMed

61. **Yamaguchi HL,** Yamaguchi Y, Peeva E (2023) Role of Innate Immunity in Allergic Contact Dermatitis: An Update. *Int J Mol Sci* **24** https://doi.org/10.3390/ijms241612975 | PubMed

62. **Lugano R,** Ramachandran M, Dimberg A (2020) Tumor angiogenesis: causes, consequences, challenges and opportunities. *Cell Mol Life Sci* **77**:1745-1770 https://doi.org/10.1007/s00018-019-03351-7 | PubMed

63. **Togashi Y,** Shitara K, Nishikawa H (2019) Regulatory T cells in cancer immunosuppression - implications for anticancer therapy. *Nat Rev Clin Oncol* **16**:356-371 https://doi.org/10.1038/s41571-019-0175-7 | PubMed

64. **Moon H,** Donahue LR, Choi E, Scumpia PO, Lowry WE, Grenier JK, Zhu J, White AC (2017) Melanocyte Stem Cell Activation and Translocation Initiate Cutaneous Melanoma in Response to UV Exposure. *Cell Stem Cell* **21**:665-678.e666. https://doi.org/10.1016/j.stem.2017.09.001 | PubMed

65. **Zaidi MR,** Davis S, Noonan FP, Graff-Cherry C, Hawley TS, Walker RL, Feigenbaum L, Fuchs E, Lyakh L, Young HA, *et al.* (2011) Interferon-gamma links ultraviolet radiation to melanomagenesis in mice. *Nature* **469**:548-553 https://doi.org/10.1038/nature09666 | PubMed

66. **Handoko HY,** Rodero MP, Boyle GM, Ferguson B, Engwerda C, Hill G, Muller HK, Khosrotehrani K, Walker GJ (2013) UVB-induced melanocyte proliferation in neonatal mice driven by CCR2-independent recruitment of Ly6c(low)MHCII(hi) macrophages. *J Invest Dermatol* **133**:1803-1812 https://doi.org/10.1038/jid.2013.9 | PubMed

67. **Gamba CA,** Swetter SM, Stefanick ML, Kubo J, Desai M, Spaunhurst KM, Sinha AA, Asgari MM, Sturgeon S, Tang JY (2013) Aspirin is associated with lower melanoma risk among postmenopausal Caucasian women: the Women's Health Initiative. *Cancer* **119**:1562-1569 https://doi.org/10.1002/cncr.27817 | PubMed

68. **Ogbechie-Godec OA,** Elbuluk N (2017) Melasma: an Up-to-Date Comprehensive Review. *Dermatol Ther* **7**:305-318 https://doi.org/10.1007/s13555-017-0194-1 | PubMed

69. **Davis EC,** Callender VD (2010) Postinflammatory hyperpigmentation: a review of the epidemiology, clinical features, and treatment options in skin of color. *J Clin Aesthet Dermatol* **3**:20-31 PubMed

70. **Ding Y,** Xu Z, Xiang LF, Zhang C (2023) Unveiling the mystery of Riehl's melanosis: An update from pathogenesis, diagnosis to treatment. *Pigment Cell Melanoma Res* **36**:455-467 https://doi.org/10.1111/pcmr.13108 | PubMed

71. **Kaufman BP,** Aman T, Alexis AF (2018) Postinflammatory Hyperpigmentation: Epidemiology, Clinical Presentation, Pathogenesis and Treatment. *Am J Clin Dermatol* **19**:489-503 https://doi.org/10.1007/s40257-017-0333-6 | PubMed

72. **Ebihara T,** Nakayama H (1997) Pigmented contact dermatitis. *Clin Dermatol* **15**:593-599 https://doi.org/10.1016/s0738-081x(97)00072-2 | PubMed

73. **Taylor A,** Pawaskar M, Taylor SL, Balkrishnan R, Feldman SR (2008) Prevalence of pigmentary disorders and their impact on quality of life: a prospective cohort study. *J Cosmet Dermatol* **7**:164-168 https://doi.org/10.1111/j.1473-2165.2008.00384.x | PubMed

74. **Ghasemiyeh P,** Fazlinejad R, Kiafar MR, Rasekh S, Mokhtarzadegan M, Mohammadi-Samani S (2024) Different therapeutic approaches in melasma: advances and limitations. *Front Pharmacol* **15**:1337282. https://doi.org/10.3389/fphar.2024.1337282 | PubMed

75. **Li JL,** Goh CC, Keeble JL, Qin JS, Roediger B, Jain R, Wang Y, Chew WK, Weninger W, Ng LG (2012) Intravital multiphoton imaging of immune responses in the mouse ear skin. *Nat Protoc* **7**:221-234 https://doi.org/10.1038/nprot.2011.438 | PubMed

76. **Stuart T,** Butler A, Hoffman P, Hafemeister C, Papalexi E, Mauck WM, Hao YH, Stoeckius M, Smibert P, Satija R (2019) Comprehensive Integration of Single-Cell Data. *Cell* **177**:1888 https://doi.org/10.1016/j.cell.2019.05.031 | PubMed

77. **Stoeckius M,** Zheng S, Houck-Loomis B, Hao S, Yeung BZ, Mauck WM, Smibert P, Satija R (2018) Cell Hashing with barcoded antibodies enables multiplexing and doublet detection for single cell genomics. *Genome Biol* **19**:224 https://doi.org/10.1186/s13059-018-1603-1 | PubMed

78. **Aran D,** Looney AP, Liu L, Wu E, Fong V, Hsu A, Chak S, Naikawadi RP, Wolters PJ, Abate AR, *et al.* (2019) Reference-based analysis of lung single-cell sequencing reveals a transitional profibrotic macrophage. *Nat Immunol* **20**:163-172 https://doi.org/10.1038/s41590-018-0276-y | PubMed

79. **Street K,** Risso D, Fletcher RB, Das D, Ngai J, Yosef N, Purdom E, Dudoit S (2018) Slingshot: cell lineage and pseudotime inference for single-cell transcriptomics. *BMC Genomics* **19**:477 https://doi.org/10.1186/s12864-018-4772-0 | PubMed

Peer reviews

Reviewer #1 (Public review):

Summary:

The immune system represents a source for melanocyte-extrinsic determinants of melanoma. Multiple immune cell types, including natural killer cells and CD8+ cytotoxic T lymphocytes, destroy cancer cells directly, and this anti-tumor activity is widely thought to eliminate many nascent tumors before they become clinically detectable. Regulatory T (Treg) cells, which are defined by expression of the transcription factor Foxp3, function as critical suppressors of lymphocyte activation in both homeostatic and disease contexts. Intratumoral Treg cell accumulation has been associated with disease progression in the clinic, and Treg cell depletion inhibits melanoma outgrowth in transplantable models of the disease.

However, the role of Treg cells during the early, premalignant stage of melanocyte expansion has not been examined. To study the interplay between incipient melanoma and cutaneous inflammation, the authors subjected an autochthonous murine model of melanoma [LSL-BrafV600E;Ptenfl/fl;Tyr::CreERT2 (BPT)mice] to three distinct inflammatory immune perturbations. Each of these perturbations accelerated premalignant melanocyte outgrowth, which was unexpected given that both Treg cell depletion and DNFB treatment markedly enhanced conventional T (Tconv) cell infiltration into the skin. Detailed analysis of each inflammatory response revealed a shared cellular and molecular signature comprising myeloid infiltration, characteristic cytokines and tissue remodeling factors, and vascular permeability. Altogether, the results support the hypothesis that oncogenic mutations in

melanocytes along with altered immune response and inflammation synergistically drive melanomagenesis.

Strengths:

(1) The use of the three distinct inflammatory immune perturbations, such as transient Treg cell depletion, acute UV- B irradiation, and 2,4-dinitrofluorobenzene (DNFB)-induced contact hypersensitivity.

(2) The re-examination of the role of Treg cells in transplantable models of tumor growth by Subcutaneous (s.c.) implantation of syngeneic B16F10 melanoma cells as widely used to study anti-tumor immunity and to interrogate the effects of Treg cells on tumor suppression.

(3) The use of the LSL-TdTomato mice for measuring the TdTomato fluorescence in each immune cell type to assess uptake of melanocyte antigen.

(4) scRNA-seq data document a broad and rapid myeloid inflammatory response in Treg cell-deficient skin.

Weaknesses:

(1) The expression of inflammatory mediators Il1b, Il6, and TNFa, and angiogenic mediators Hif1a and Ang2 in all of the three models of immune perturbation has been verified at the transcript level by qRT-PCR, and it remains to be determined whether it correlates with the same at the protein level.

(2) scRNA-seq data to profile the diversity of immune cells (CD45+) in the ear skin of the DNFB-treated contact hypersensitivity model are currently missing.

(3) The authors indicate that at least 2 prior studies directly implicated inflammatory macrophages in the melanocyte proliferation response. However, no attempts were made for the identification of the UVB-driven factors underlying myeloid recruitment by which these cells activate melanocytes.

(4) It is very surprising to observe that altered immune responses, such as enhanced Tconv cell priming and activation in Treg cell-deficient skin, failed to antagonize mutant melanocyte outgrowth in the BPT model. While UVB-induced skin inflammation differs somewhat from the response to Treg cell depletion, both feature the infiltration of tissue remodeling macrophages and vascular instability. The findings that contact hypersensitivity can promote the expansion of non-malignant BRAF (V600E)Pten- Het melanocytes have interesting implications for benign hyperpigmentation conditions, such as post-inflammatory hyperpigmentation, Riehl's melanosis, and melasma.

https://doi.org/10.7554/eLife.112061.1.sa2

Reviewer #2 (Public review):

Summary:

Tran and colleagues investigate how inflammation alters the earliest stages of melanoma tumorigenesis in mice carrying LSL-BrafV600E, Ptenfl/fl, and Tyr-CreERT2 alleles. They compare transient regulatory T cell depletion, acute UVB irradiation, and DNFB-induced contact hypersensitivity. Each perturbation increases ear pigmentation and Tyrp1 expression after oncogene induction. The inflammatory settings also share recruitment of monocytes and macrophages, expression of inflammatory and tissue-remodeling programs, and increased vascular permeability. Dexamethasone attenuates the DNFB-associated phenotype. A secondary finding of particular interest is that regulatory T cell depletion accelerates the premalignant BPT phenotype but inhibits B16F10 tumor growth, suggesting that regulatory T

cells can have different effects during tumor initiation and established transplantable disease.

The study addresses an important question that is difficult to approach using transplantable tumor models. The data convincingly show that each perturbation produces substantial inflammation in the skin and that vascular leakage accompanies the response. At present, though, the central biological endpoint is not sufficiently separated from melanogenesis. Darkening of the ear and increased Tyrp1 RNA can reflect more pigment or altered differentiation within the existing oncogene-carrying melanocytes rather than an increase in their number, particularly given that pigment content is itself variable in transformed melanocytes, which range from heavily pigmented to nearly amelanotic. This issue is especially important in the UVB and DNFB experiments, where inflammatory signals can alter pigmentation directly.

Strengths:

The autochthonous BPT model is a major strength. It preserves the native relationship between melanocytes and the surrounding stromal and immune compartments during lesion initiation. Including three distinct inflammatory perturbations makes the recurring association with melanocyte-associated readouts more persuasive than any single model would be. The paired-ear DNFB design is efficient and controls for inter-animal variability. The combination of flow cytometry, single-cell RNA sequencing, intravital imaging, and Evans Blue assays provides useful complementary evidence that the inflammatory interventions remodel the local tissue environment. The B16F10 experiments help establish that the unexpected effect of regulatory T cell depletion is specific to the early autochthonous setting rather than a general failure of the depletion model. The BT-Het experiment is also thoughtful in asking whether inflammation can enhance the phenotype of oncogene-carrying melanocytes in a nevus-stage context that does not proceed to full malignant progression after oncogene induction alone.

Weaknesses:

The strongest caveat concerns the central claim. The outgrowth readouts are ear darkening and bulk Tyrp1 expression, but both may report pigment or differentiation state rather than the number of oncogene-carrying melanocytes. Pigment content is not a reliable proxy for cell number here, since the same population can darken or lighten without any change in cell number. No direct count or lineage-reporter measurement is provided for the regulatory T cell, UVB, or DNFB comparisons. Until that gap is filled, the data support increased pigmentation of oncogene-carrying melanocytes more firmly than the premalignant expansion named in the title, and this concern is most pronounced in the UVB and DNFB settings, where inflammation can change pigmentation on its own.

Secondly, the proposed shared mechanism is largely associative. Dexamethasone appropriately shows that inflammation as a whole is required for the DNFB phenotype, but as a broad anti-inflammatory it cannot isolate any single component. The manuscript singles out blood vessel remodeling as particularly important, and that specific attribution exceeds what a non-selective drug can show, especially as no individual pathway is selectively blocked in a tumor-initiation experiment and Il6 is reduced only modestly. The authors acknowledge that the precise chain of causation is unresolved, so the vascular claim should be softened to match or tested directly.

Also, several of the mechanistic conclusions rest on thin or single cohorts and on single-cell data whose replication is not fully reported, making them less convincing than the inflammatory phenotypes themselves. The systemic regulatory T cell model shows the consequences of body-wide depletion rather than a skin-specific regulatory T cell function, and the inferred monocyte-to-macrophage trajectory reflects transcriptional similarity rather

than a demonstrated lineage path. The interpretation of dendritic-cell TdTomato uptake as evidence of antigen presentation or T cell priming is not supported by a direct measure of reactivity.

Finally, the nevus-stage framing should be corrected. The manuscript frames the BT-Het experiment as testing non-oncogenic conditions, but those melanocytes carry BrafV600E, so it is better read as inflammation-enhanced behavior of oncogene-carrying melanocytes at the nevus stage.

https://doi.org/10.7554/eLife.112061.1.sa1

Reviewer #3 (Public review):

Summary:

Tran et. al. investigate how inflammation in the skin influences the early stages of melanomagenesis. They use an autochthonous, tamoxifen-inducible mouse melanoma model (LSL-BrafV600E;Ptenfl/fl;Tyr::CreERT2, "BPT") to examine three inflammatory perturbations: transient depletion of regulatory T cells, acute ultraviolet-B irradiation, and contact hypersensitivity induced by 2,4-dinitrofluorobenzene (DNFB). They report that each perturbation promotes the recruitment of immune cells, especially inflammatory monocytes and macrophages, increased expression of inflammatory and tissue-remodeling factors, and enhanced vascular permeability, which ultimately increases the outgrowth of premalignant melanocytes measured by local pigmentation and expression of the melanocyte-associated gene Tyrp1. In the DNFB model, the authors showed that treatment with dexamethasone reduces the effects of contact hypersensitivity on pigmentation, inflammatory gene expression, and vascular leakage, potentially providing a translational angle.

Strengths:

An interesting observation is that transient Treg depletion promotes premalignant melanocyte outgrowth in the autochthonous BPT model while inhibiting the growth of transplantable B16 F10 tumors. This contrast is consistent with a role for Tregs in limiting inflammatory disruption of the skin during early tumorigenesis and highlights the value of autochthonous models. These findings may also have broader implications for understanding the stage- and context-dependent functions of Tregs in cancer.

Another strength of this manuscript is the comparison of three mechanistically distinct inflammatory perturbations. Treg depletion, UVB irradiation, and DNFB-induced contact hypersensitivity engage different inflammatory pathways but converge on myeloid-cell recruitment, inflammatory gene expression, and increased vascular permeability. This convergence strengthens the conclusion that an acute inflammatory microenvironment is associated with enhanced melanocyte outgrowth during the early premalignant phase.

Weaknesses:

The paper convincingly establishes a correlation between the inflammatory signature and melanocyte outgrowth across three distinct perturbations. However, the mechanistic claim that myeloid cells and/or vascular remodeling drive melanocyte expansion rests primarily on the dexamethasone experiments in the DNFB model. Because dexamethasone broadly affects immune, stromal, endothelial, and melanocytic compartments, these experiments do not establish that inflammatory monocytes/macrophages or vascular destabilization are specifically required for the melanocyte response.

A related limitation is that the proposed monocytic origin of the inflammatory macrophage population following perturbation remains inferred. Although the scRNA-seq data and pseudotime analysis in Figure 4 - Supplement 2 are consistent with a trajectory from

monocytes to macrophages, they do not exclude local reprogramming of resident macrophages into an inflammatory state. This alternative is particularly relevant because resident macrophage populations have been implicated in vascular remodeling and tumor outgrowth (PMIDs: 36493773 and 40216154).

Finally, the assessment of melanocyte outgrowth is largely through increased pigmentation and whole-ear Tyrp1 expression. Although these measurements may reflect increased melanocyte abundance, they may also be influenced by melanogenic activity or increased Tyrp1 expression per cell. More direct evidence of melanocyte proliferation, such as Ki67 or EdU/BrdU staining specifically within TdTomato-positive melanocytes, would support the use of "expansion" and "proliferation" throughout the manuscript. Histopathological characterization of lesion architecture, atypia, proliferation, and invasion would also help establish the premalignant nature of the lesions.

https://doi.org/10.7554/eLife.112061.1.sa0